

TECHNOLOGY DEVELOPMENT FOR EXOPLANET MISSIONS

Technology Milestone Whitepaper
Part 1

OPTICAL AND MECHANICAL VERIFICATION OF AN EXTERNAL OCCULTER FOR STARLIGHT SUPPRESSION

PROF. N. JEREMY KASDIN
PRINCIPAL INVESTIGATOR
PRINCETON UNIVERSITY
MECHANICAL AND AEROSPACE ENGINEERING

October, 2015

CoInvestigators:

Robert Vanderbei, Princeton University; Doug Lisman (Institutional PI), Stuart Shaklan, Mark Thomson, Jet Propulsion Laboratory, California Institute of Technology.

Other Key Personnel:

Dan Sirbu, Yunjong Kim, Princeton University
Eric Cady, David Webb, Jet Propulsion Laboratory, California Institute fo Technology

Document #: 1499977

Approvals

Released by:



11/13/2015

N. Jeremy Kasdin
Principal Investigator, Princeton University

Approved by:

Nicholas Siegler
Exoplanet Exploration Program Chief Technologist, JPL

Douglas Hudgins
Exoplanet Exploration Program Scientist, NASA HQ

CONTENTS

1. Objective	4
2. Experiment Overview and Laboratory Scaling	5
3. Previous Experimental Results	7
3.1. Previous Experiment Design	7
3.2. Previous Experiment Results	8
3.3. Diffractive Analysis	11
4. New Experiment Design	13
4.1. Scaled Occulter Mask Design	13
4.2. Laboratory Scaling	15
4.3. Predicted Performance	17
4.4. Experiment Design	27
5. Success Criteria	28
6. Certification	30
7. Work Plan and Schedule	31
8. List of Acronyms	32
References	33

1. OBJECTIVE

A major science goal of the exoplanet research community is the detection and characterization of Earth-like planets. It is a central component of the NASA strategic plan and one of the top three science objectives in the ASTRO 2010 decadal survey. Nevertheless, doing so is a formidable task; planets are much fainter than their host stars and are often at small angular separations. In particular, Earth-like planets—that is, rocky planets in habitable zones—are estimated to be 10^{10} times dimmer than the stars they orbit and to be located at angular separations of a hundred milliarcseconds or less from the closest stars. Many approaches have been suggested over the last couple of decades for imaging these planets, including nulling interferometers, both structurally connected and free-flying, pupil interferometers, various types of coronagraphs, and external occulters. All have their advantages and disadvantages and all are at various levels of technological readiness. An important objective of NASA’s exoplanet program is to advance the technological readiness of the most promising approaches for exoplanet imaging so an informed choice can be made later this decade and progress can begin on an integrated observatory design.

We focus in this project on external occulters, or starshades, for achieving the needed starlight suppression. Our goal is to provide NASA with a viable low risk mission option that will be ready for mission development later in the decade. To that end, we have been performing technology development on all critical aspects of occulter development. In this successor Technology Development for Exoplanet Missions (TDEM) project, part of the ROSES Strategic Astrophysics Technology program, we further advance the technology by optical verification of starlight suppression at a laboratory scale and by building a second-generation flight-like starshade petal with sharp optical edges to minimize solar scatter.

There are many challenges associated with starshade development and use. Most critical are 1) manufacturing an occulter to the required shape and meeting precise tolerances, 2) manufacturing the petal edges with small enough radius of curvature to minimize sunlight scatter into the telescope, 3) deploying the occulter central disk and petals while meeting the tight positioning requirements, 4) understanding and controlling the thermal deformations of the petals across the mission lifetime, 5) verifying in the laboratory that the optical modeling sufficiently captures the diffraction, and 6) demonstrating that the occulter can be precisely aligned with the telescope during an observation. Our first two successful TDEMs addressed the first and third. We showed that an occulter petal can be built to the required tolerances, and measured, consistent with an overall contrast of 10^{-10} [1]. We also showed that a set of subscale petals on an existing truss can be repeatedly deployed with the required positioning accuracy.

The second and fourth are currently being addressed in separate projects at JPL and subcontractors. In this TDEM we address challenge (5) and revisit challenges (1) and (2). In this first part of a two-part white paper we describe our plans to upgrade the laboratory at Princeton University to optically verify scaled starshade masks with the same characteristics as a flight system and reduced manufacturing error to minimize the scatter and diffraction due to the small size of the test article. In Part II of the white paper we describe our plans to build a second, full-scale flight-like petal to flight tolerances (as in our first TDEM) but this time incorporating a flight-like edge and design upgrades.

Our objective in the first part is to optically verify the scalar field models being used to design starshades and predict mission performance. To that end, our specific milestone is to

TDEM Occulter Milestone:

- Confirm that the measured suppression and contrast after the laboratory mask matches or bests the predicted $1e-9$ suppression and corresponding contrast of the scalar diffraction model, in a sub-scale laboratory experiment at Flight-like Fresnel number, measured at 3 wavelengths in the band 500-850 nm.

This milestone will demonstrate that the Fresnel-Huygens scalar diffraction theory used to both predict starshade performance (suppression and contrast) and verify requirements is a sufficiently accurate physical model to predict performance of the space system over the large range of intensities considered. By demonstrating high suppression experimentally at a flight-like Fresnel number, we will have validated the same model as used on the flight system. Since an end-to-end optical verification of a flight system is not possible, final validation will be done by measuring the various errors in the error budget and using our now verified models to demonstrate ultimate compliance with the performance goals.

2. EXPERIMENT OVERVIEW AND LABORATORY SCALING

Since occulter for any size mission are typically tens of meters across with tens of thousands of kilometers separation, testing them at full scale is not possible. All methods for verification of starshade performance rely on modeling. That is, since it is impossible to do *in situ* optical tests of a full scale occulter to verify that the designed-for starlight suppression is achieved, we instead make measurements of the occulter shape and infer the resulting suppression via our optical models. This requires that those models be validated to give confidence in our predicted performance.

To validate the models, we design subscale experiments which obey the same scalar field relationship—at least out to some desired radius beyond which we aren't concerned—and verify the performance within this radius. One of the challenges of such a laboratory experiment is scaling the starshade/telescope system by many orders of magnitude while maintaining meaningful results. This is achieved by scaling the separation distance z , the radius r in the occulter plane, and the radius ρ in the telescope pupil plane, such that the dimensionless Fresnel numbers appearing in the diffraction integral ($N_o = \frac{r^2}{\lambda z}$ and $N_t = \frac{\rho^2}{\lambda z}$) remain constant. This guarantees that the mathematical, integral representation of the diffraction past the starshade is identical for both the full-scale and lab-size geometries within the Fresnel-Huygens scalar diffraction approximation. That is, we start with the expression for the electric field E_{ap} past an occulter mask with circularly symmetric transmittance profile $A(r)$ with range $[0, 1]$ at a distance z downstream at wavelength λ , given by the Fresnel integral [2]:

$$(1) \quad E_{ap}(\rho) = \frac{2\pi}{i\lambda z} e^{\frac{\pi i}{\lambda z} \rho^2} \int_0^R e^{\frac{\pi i}{\lambda z} r^2} J_0\left(\frac{2\pi r \rho}{\lambda z}\right) A(r) r dr$$

where R is the maximal radial extent of the mask, J_0 is the zeroth-order Bessel function of the first kind, ρ is the radial distance across the shadow, and r is the radial distance across the occulter mask. We then make the substitutions $\rho' = \rho/s$, $r' = r/s$, $A'(r') = A(sr')$, $z' = z/s^2$, $R' = R/s$, and $E'_{ap}(\rho') = E_{ap}(s\rho')$ to derive the scaled version,

$$(2) \quad E'_{ap}(\rho') = \frac{2\pi}{i\lambda z'} e^{\frac{\pi i}{\lambda z'} \rho'^2} \int_0^{R'} e^{\frac{\pi i}{\lambda z'} r'^2} J_0\left(\frac{2\pi r' \rho'}{\lambda z'}\right) A'(r') r' dr',$$

which is functionally identical to the unscaled expression.

The resulting scaling is quadratic along the separation direction and linear in the transverse directions, allowing us to scale a space occulter to lab size. It is worth noting that under this scaling, the geometry does change so the inner working angle that we would expect from space increases in the laboratory substantially. However, the mathematical descriptions of the lab and space versions are identical. The scaling approach is thus an effective means of demonstrating that the scalar theory and resulting mathematical description is valid.

To eliminate a potential source of optical error, we also change the geometry to use a diverging beam. This avoids introducing aberrations from collimating optics that would corrupt the wavefront impinging on the starshade mask. This is done by introducing a scaling factor $\gamma > 1$ applied as a

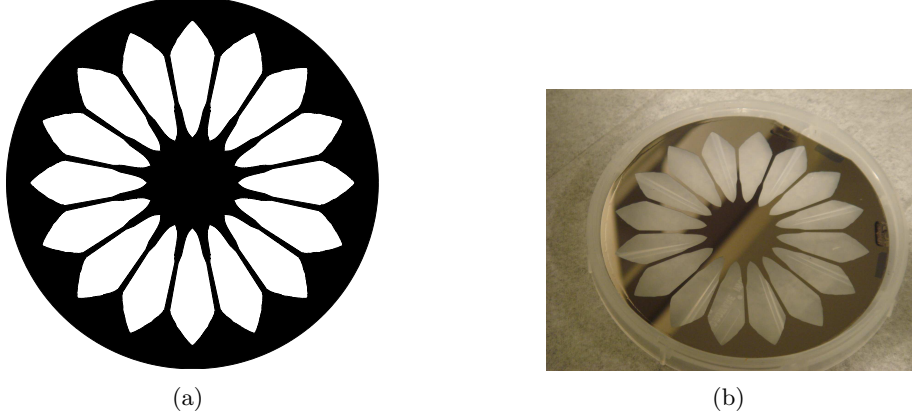


FIGURE 1. (Left) The occulter mask. (Right) The silicon mask.

change of variables $r'' = r'/\gamma$, $\rho'' = \gamma\rho'$, and $z'' = z'$:

$$(3) \quad E''_{\text{ap}}(\rho'') = \frac{2\pi\gamma^2}{i\lambda z'} e^{\frac{\pi i}{\lambda z'} \frac{\rho''^2}{\gamma^2}} \int_0^{R''} e^{\frac{\pi i}{\lambda z'} \gamma^2 r''^2} A''(r'') J_0\left(\frac{2\pi r'' \rho''}{\lambda z'}\right) r'' dr''.$$

Substituting $\gamma^2 = 1 + z'/h$ gives

$$(4) \quad E''_{\text{ap}}(\rho'') = \frac{2\pi\gamma^2}{i\lambda z'} e^{\frac{\pi i}{\lambda z'} \frac{\rho''^2}{\gamma^2}} \int_0^{R''} e^{\frac{\pi i}{\lambda} \frac{r''^2}{z'}} e^{\frac{\pi i}{\lambda} \frac{r''^2}{h}} A''(r'') J_0\left(\frac{2\pi r'' \rho''}{\lambda z'}\right) r'' dr''.$$

Except for the leading phase factor, the expression is identical when a spherical input beam is considered:

$$(5) \quad E''_{\text{in}}(r'') = \frac{1}{\sqrt{h^2 + r''^2}} e^{\frac{2\pi i}{\lambda} \sqrt{h^2 + r''^2}}$$

$$(6) \quad \approx \frac{1}{h} e^{\frac{2\pi i}{\lambda} h} e^{\frac{\pi i}{\lambda} \frac{r''^2}{h}}.$$

One of the most significant challenges in creating a laboratory-scale experiment is eliminating diffraction and specular reflection from mounting supports for the starshade model. This was a significant source of error in past experiments. [3, 4, 5] Our approach to mitigating this diffraction problem is to create a second ring around the outside of the occulter so that the open region is an annulus. By putting a smooth attenuation on the outside of this annular opening similar to that on the starshade portion, we create an edge that interferes negligibly with the high-contrast central regions of the shadow. We then support the central starshade with the same number of struts as petals to ensure that any diffracted light appears outside the shadow. (See [6] for details.) This allows us to mount the starshade in a baffling screen with light only passing through the annulus, eliminating both diffraction from the supports and stray light. While this does introduce an outer working angle beyond which there is another shadow with no light, we are able to fully verify the diffraction of the starshade at the critical small separations near the inner working angle by examining the annular suppressed region.

Figure 1 shows the design of the previous lab mask (Fig. 1(a)) and the experiment silicon mask used for our previous results (Fig. 1(b)). [7, 8] The masks we have used are manufactured at the Microdevices Lab (MDL) at JPL from standard 101.6 mm in diameter and 400 μm thick silicon wafers using Deep Reactive Ion Etching (DRIE). They are thinned to 50 μm in the vicinity of the openings and then etched through for the final mask (resulting in 50 μm sidewalls around the edges of the mask). The mask is then coated with aluminum to ensure it is opaque at all wavelengths of interest.

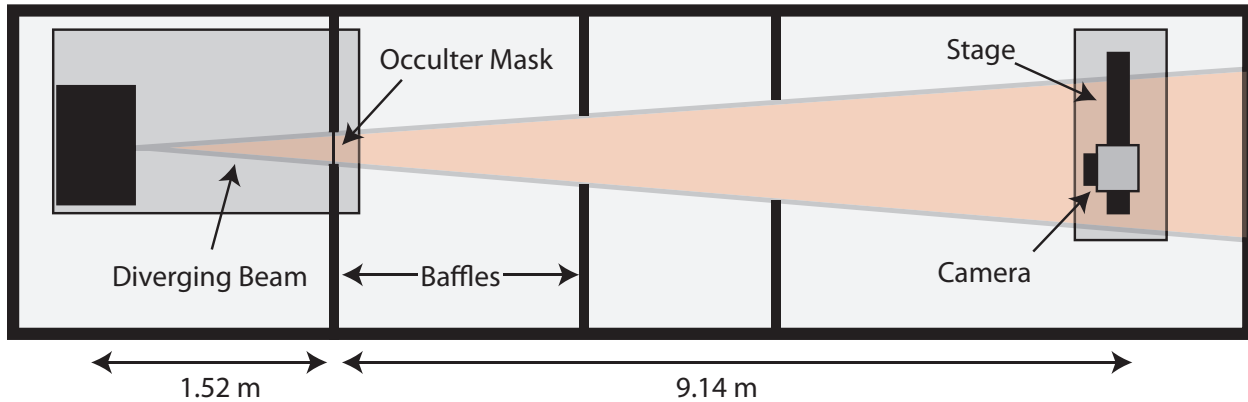


FIGURE 2. The layout of the occulter testbed.



FIGURE 3. *Left:* The occulter camera with baffling. *Right:* Photo of the occulter experiment enclosure in the Gas Dynamics Lab at the Princeton Forrestal Campus.

3. PREVIOUS EXPERIMENTAL RESULTS

3.1. Previous Experiment Design. Laboratory scaled experiments have been ongoing at Princeton for several years. The current occulter testbed at Princeton consists of a set of optics simulating a star-occulter-telescope system; a schematic layout is shown in Fig. 2. The experiment is located inside a 40'×4'×8' enclosure, which is sealed to prevent stray light from entering, and baffled at 8' intervals down the length of the enclosure. A HEPA filter runs continuously to reduce airborne particulates. Two Newport optical tables are placed at either end to hold the optics. All isolation on the tables is passive. The first table is 30"×72", long enough to put both the point source and the occulting mask on the table. The second is a smaller workstation, 30"×30", small enough to be moved easily by two people as necessary. Pictures of the facility are in Fig. 3.

We use two different light-sources in the experiment. One source is a single-mode 2 mW HeNe laser operating monochromatically at 632 nm. To create the diverging beam, the beam is passed through two lenses acting as a beam expander, and focused onto a 15 μm pinhole through an off-axis parabolic mirror. We use a diverging beam through a pinhole so that the pinhole acts as a spatial filter that removes high-frequency aberrations due to surface error on the optics. The choice of lenses and pinhole affects the divergence angle of the beam. Alternatively, we also use a

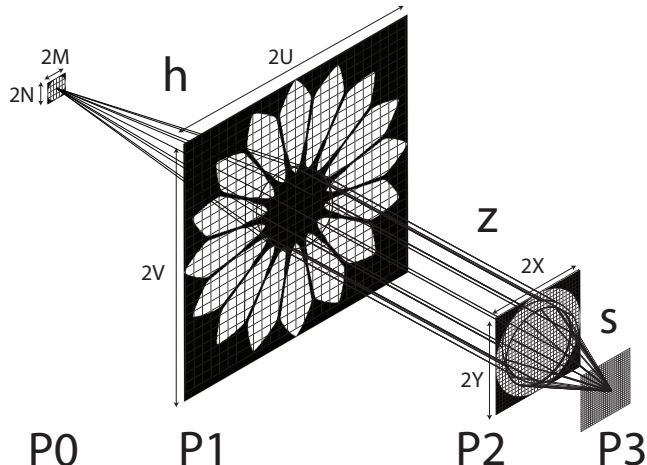


FIGURE 4. Optical planes for the occulter testbed. The diverging beam is at P0 and is incident on the occulter mask at P1. The shadow is directly measured at P2 in terms of *suppression*, and the point-spread function of the system is measured at P3 in terms of *contrast* via a telephoto lens attached to the camera.

two-channel fiber-coupled laser source (520nm at 10 mW and 638nm at 15 mW) with the diverging beam output from a matched single-mode fibre. The diverging beam propagates 1.5 m before encountering the occulter mask which it overfills at the end of the optical table. Baffles are placed around the occulter mask extending to the walls of the enclosure and a further two sets of full wall baffles are located downstream to minimize stray light reflection. The mask is tilted 5° to eliminate a ghost reflection by directing the back-reflection into a black foil beamdump.

Beyond the occulter mask, the beam propagates 9.1m to the second optical table on which a camera is placed on two 300 mm long-travel stages; both move perpendicular to the propagation direction, one horizontally and one vertically. Together these stages allow the camera to be precisely aligned in the shadow cast by the occulter. The camera is an astronomical-grade thermoelectrically cooled Starlight Xpress SXV-H9 CCD. A telephoto lens set at $f = 300$ mm can be outfitted via the M42 mount, and the smallest available aperture setting at $f/22$ is used to form a six-bladed iris. The CCD has pixel pitch of $6.45 \mu\text{m} \times 6.45 \mu\text{m}$.

3.2. Previous Experiment Results. The optical planes that define the occulter testbed are illustrated in Figure 4. The diverging beam is located at P0 and is incident on the occulter mask at P1. The shadow propagates from P1 to P2, the telescope’s pupil plane. The telescope’s image plane is at P3.

We define two key metrics that define the performance of our testbed. *Suppression* is measured at the pupil plane (P2) with a lensless camera. Suppression is the ratio of the flux in the mask’s shadow to the flux without the mask. This measurement is taken by first centering the camera in the shadow of the occulter mask without the lens attached and taking long exposures; then the mask is removed and short exposures are retaken. It measures the performance of the occulter directly and is decoupled from the telescope. *Contrast* is measured at the image plane (P3) with a camera focused on the point source at P0, and is the ratio between the flux at each pixel in the image formed when the mask is in place and the flux of the peak pixel of the point spread function without a mask. Performance depends on aperture size. Measuring both suppression and contrast is useful as it allows for verification of the consistency of the results; contrast measurements can reveal the sources of limitations of the suppression performance of the occulter mask, as the source of any stray light can be directly observed.

Parameter	Laboratory	Space Equivalent
Pinhole-to-occulter distance	1.5 m	Infinity
Occulter-to-camera distance	9.1 m	97,000 km
Radius of dark zone	13 mm	12 m
Occulter diameter	44 mm	376 m
Outer occulter diameter	88 mm	N/A
Inner working angle	8.4 arcmin	400 mas
Outer working angle	17 arcmin	N/A
Telescope diameter	14 mm	17 m
Wavelength suppression band	400-1100 nm	400-1100 nm

TABLE 1. Summary of optimization parameters for inner and outer occulter shape design for current testbed.

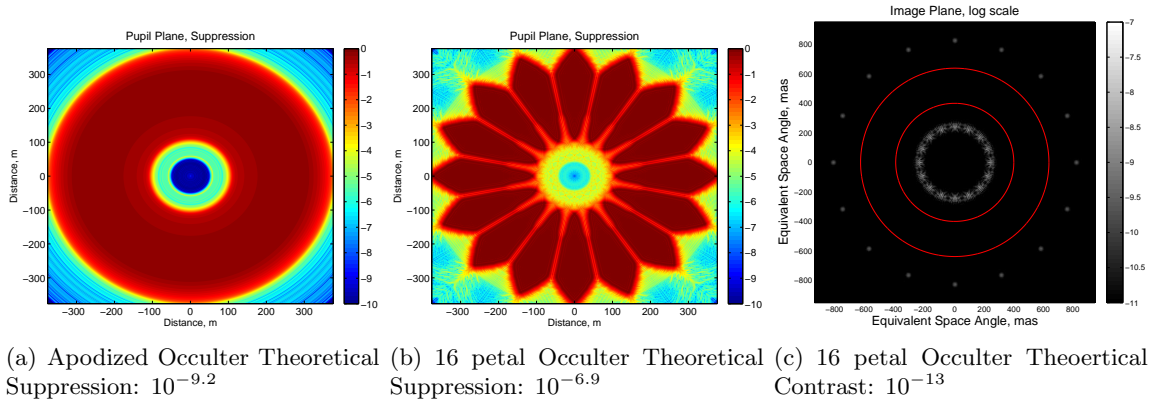


FIGURE 5. Theoretical performance of current laboratory occulter design.

The limitations of the size of our current laboratory forced a scaled design that was equivalent to a significantly larger space occulter and an extremely large telescope, with a correspondingly much larger inner working angle. This has been true for most experiments to date. Table 1 presents the design parameters of our scaled lab experiment and the space equivalent occulter. This design has an equivalent Fresnel number of 607.3 at 600 nm, compared to the typical mission being considered with a Fresnel number of roughly 15. The consequence of this disparity is a highly over-resolved image that can produce very high contrast even in the face of limited suppression in the shadow.

Figure 5 shows the theoretical suppression and contrast of the design for the masks in Fig. 1. Notable is the significant loss in suppression past the petalized version (Fig. 5(b)) compared to the ideal apodized design (Fig 5(a)). This exposes a need for many more petals to approach the ideal apodized suppression performance at this unusually high Fresnel number. Nevertheless, as shown in Fig. 5(c), the oversizing of the camera at this high Fresnel number results in a high resolution image with steep dropoff in the PSF, creating an average contrast below 10^{-13} .

Figure 6 shows the image plane results for the optimized occulter mask in Fig. 1, both experimental (blue) and theoretical (black). The experimental measurement curve represents the azimuthal median across 16 wedges inside the dark annular region (excluding the bright struts). A 95% confidence interval for the median based on percentile populations is shown in red. The measured median contrast across the wedges at the inner working angle of 400 mas space-equivalent is 1.05×10^{-10} and this improves towards the outer working angle of 638 mas space equivalent to 2.51×10^{-11} . Nevertheless, the optimized occulter performs significantly worse than the theoretical diffraction analysis. At 400 mas space-equivalent the theoretical median contrast is 2.19×10^{-13}

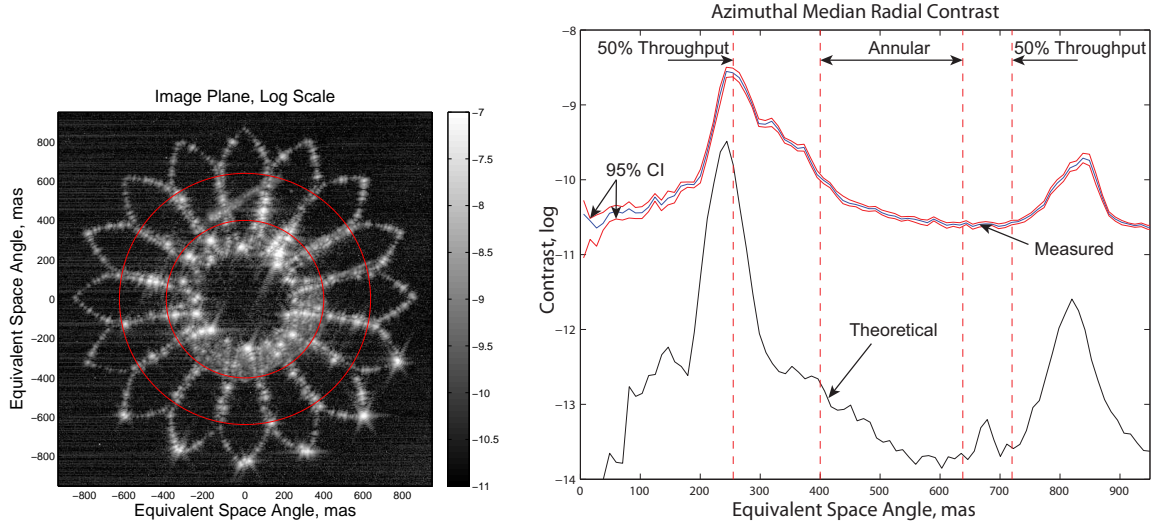


FIGURE 6. (Left) The measured point spread function for the occulter mask in the current lab. (Right) An Azimuthal cross section through the experimental image compared to the theoretical response.

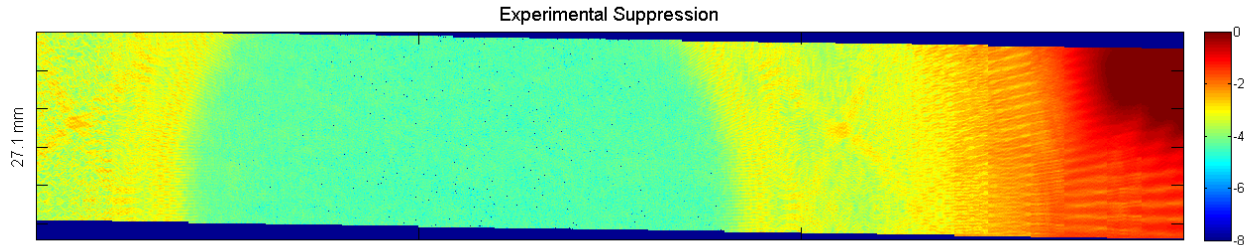


FIGURE 7. Suppression measurements are taken at the pupil plane. Here a mosaic taken with monochromatic 632 nm light is obtained by stitching images at 5mm intervals. Suppression measurements at the centre of the image for three different wavelengths are as follows: $10^{-4.74}$ for 520nm, $10^{-4.82}$ for 633nm, and $10^{-4.77}$ for 638 nm.

while at 638 mas space-equivalent the theoretical median contrast is 2.24×10^{-14} . This represents a two to three order of magnitude discrepancy.

For measuring the suppression at the pupil plane, the telephoto lens is removed from the camera. The camera is mounted on two 300-mm long travel stages that can scan the shadow. We obtained a mosaic as shown in Figure 7 by stitching together a set of frames collected at 5mm horizontal intervals across the shadow. A series of frames with different exposures are collected so as to maintain the camera's pixels in the linear regime. The actual suppression measurements at the centre of the dark shadow obtained using the 632nm laser consists of 500 frames of 300 sec exposure; each were stacked and a 50 frame median-combined dark at equal exposure was subtracted. To obtain a measurement of suppression in the dark hole, 50 calibration frames at 0.05 sec were obtained with the mask moved along the line-of-sight to the pinhole through the annular openings. A mean suppression of $10^{-4.82}$ is reported by dividing the flux for each pixel in the long-exposure stacked frames by the peak pixel flux when in direct line-of-sight to the pinhole. Similar measurements were taken at two different wavelengths with two different channels of the fibre-coupled laser with $10^{-4.74}$ for the 520nm channel and $10^{-4.77}$ for the 638 nm channel.

TABLE 2. Summary of realistic error parameters for diffractive simulation of laboratory environment.

Error Parameter	Estimated Value
Feature accuracy, δR	2.41 μm
Edge perturbations	3.1 μm RMS
Optics aberrations, $\sigma_{\text{pin,RMS}}$	$\lambda/4 \approx 160$ nm RMS
Wavefront aberrations, $\sigma_{\text{occ,RMS}}$	3 nm RMS
Diagonal beam misalignment	4.1 mm
Mask tilt	5 deg

3.3. Diffractive Analysis. The results shown in Fig. 6 prompted a careful diffractive analysis to isolate the sources of the suppression limitation and the glowing edges. This was done by moving away from the idealized one-dimensional simulations that assumed circular symmetry to a full two-dimensional (2D) propagation model. A detailed description of the computational approach can be found in Sirbu et al. [7, 8]. This computational ability was then used to analyze the effects of various errors in the experiment.

By far the most significant source of error is the manufacturing accuracy of the mask. When converting the mask’s apodization profile for CAD specifications for etching of the silicon wafer, the output consists of 16 different sets of points with each defining a polygon that represents one petal opening of the occulter mask. The spacing along the edges represents the accuracy with which the polygon is defined—a small number of points results in longer straight edges which can introduce additional diffraction leakage along the occulter edges. The process used for the lab mask shown in Fig. 1 had a feature size of approximately 2.4 microns. In addition, using spot microscope imaging of the mask, we measured a random mask edge error of approximately 3.1 micron RMS.

In addition to the manufacturing error, we included estimates of optical aberrations, misalignments of the input beam, wavefront aberrations due to air movement and temperature variations, and a five degree tilt of the mask. Details can be found in [7]. A summary of the included error parameters is given in Table 2. Figures 8 and 9 show a comparison of the experimental measurements with the final image plane simulations combining all experimental errors. Qualitatively, we observe that the overall contrast level is modeled very well by the diffractive analysis. The edges appear to be very uniform, which is similar to the experimental image; however, the experimental image exhibits several brighter spots along the contour which may be suggestive of larger defects. Additionally, some of the tips appear brighter along the tilt axis which is not the case for the diffractive model. We speculate that these are due to specular reflections from clipping due to the mask mounting bracket. The next generation of masks are being made from larger wafers that will allow a larger mount, avoiding clipping of the openings.

For a more quantitative comparison we extract the azimuthal median across a set of 16 wedges as shown in Fig. 9. The experimental results are compared to the theoretical performance of a perfectly realized 16-petal occulter mask corresponding to the simulation in Fig. 5(c). Next, we introduce only the feature size error, and lastly we introduce the 3.1 μm RMS edge perturbations and all other errors. The resulting profile has diffractive peaks that dominate the suppression performance within excellent agreement. The contrast in the dark annular regions is about a half an order of magnitude worse than modeled. This final discrepancy can be attributed to some of the brighter points across the struts which may be due to localized defects. Lastly, in Table 3 we summarize the suppression performance across all measured wavelengths and compare to the theoretical performance of a perfectly realized mask and with the modeled stochastic errors. This shows that, to high accuracy, our models predict both the suppression and contrast performance of the current mask.

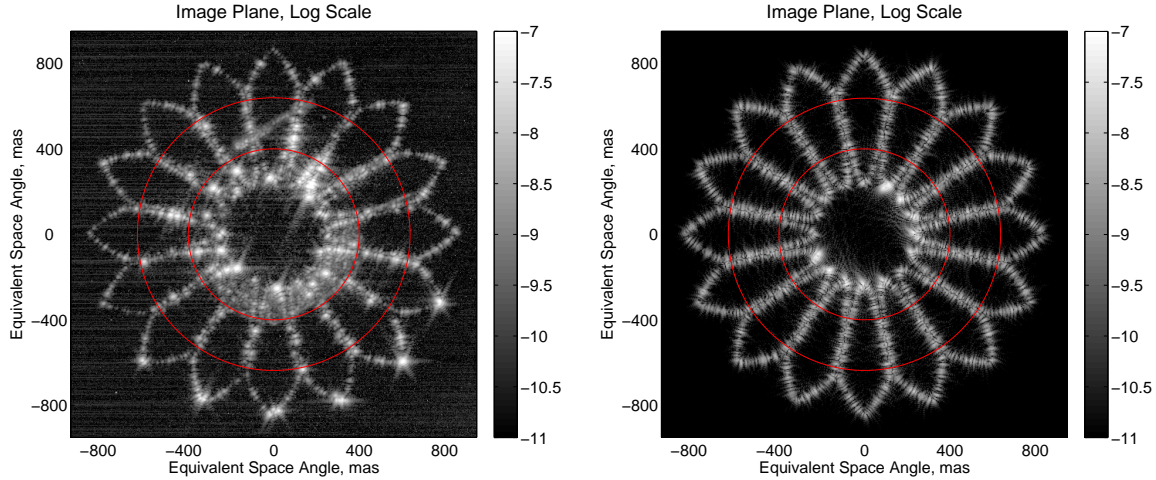


FIGURE 8. (Left) The measured point spread function for the occulter mask in the current lab. (Right) The corresponding theoretical point spread function including all modeled errors.

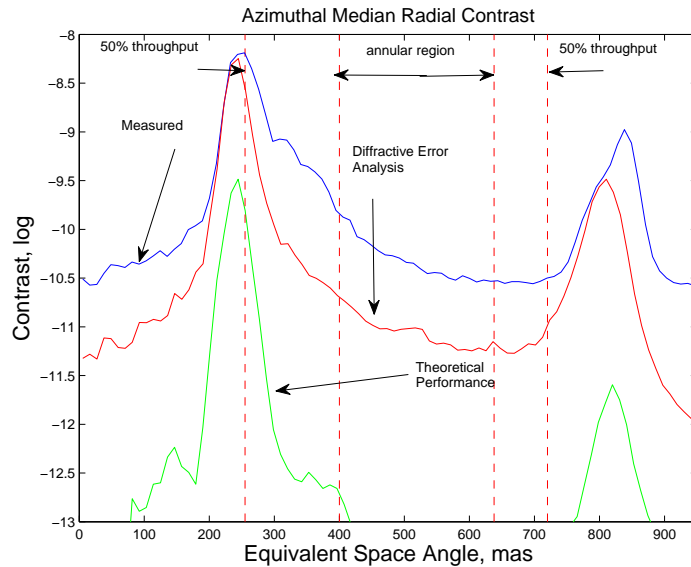


FIGURE 9. Azimuthally averaged cross section of experimental and modeled image.

While this previous round of experiments was very informative regarding the challenges and performance of scaled laboratory experiments, and gave us high confidence in our modeling approaches, Table 3 shows that we are far from achieving the desired, designed for suppression in the lab. Though our models predict the achieved suppression quite accurately, there is a need for model validation at the high-suppression level of better than 10^{-9} and at flight Fresnel numbers. This can be accomplished through more careful control of the experiment and through much higher precision in the mask manufacturing. Current estimates reveal that masks can be manufactured to better than 0.5 micron resolution with similar random errors; preliminary results in our existing lab on higher precision masks indicate that this improvement can be achieved.

Wavelength	Ideal Model	Stochastic Model			Measured
		Low	Mean	High	
520 nm	-7.48	-4.95	-4.78	-4.61	-4.74
633 nm	-6.90	-5.05	-4.93	-4.80	-4.85
638 nm	-6.89	-5.03	-4.91	-4.75	-4.77

TABLE 3. Summary of suppression performance results in our original lab operating at high Fresnel number when comparing the ideal (one-dimensional) model with the 5th percentile, mean, and 95th percentile of the Monte Carlo simulations with the (two-dimensional) model with all errors included along with the experimental results.

TABLE 4. Summary of operational Fresnel numbers for different occulter designs.

Design	Occulter Radius	Scaled Separation	Wavelength	Fresnel Number
THEIA	20 m	55,000 km	600 nm	12.1
O3	15 m	21,000 km	600 nm	17.9
Space Tech. Demo.	2.5 m	670 km	600 nm	15.5
Exo-S	15 m	30,300 km	600 nm	12.4
Current Lab Mask	188 m	97,000 km	600 nm	607.3
New Experiment	21.9 m	55,000 km	600 nm	14.5

Likewise, there is a need for experiments at the much smaller Fresnel number associated with a real flight system. This will eliminate reliance on the large resolving power of the camera for achieving high contrast and instead reflect the more realistic geometry of a flight system. The next section describes our experiment design for this TDEM to support the milestone of achieving high suppression and high contrast at flight-like Fresnel numbers.

4. NEW EXPERIMENT DESIGN

The goal of this TDEM is to build a new experimental facility that allows testing of a scaled occulter at flight-like Fresnel numbers. That scaling will also allow us to design and manufacture masks with the needed suppression of close to 10^{-10} and a flight-like number of petals, rather than the several hundred petals necessary to achieve high suppression at our previous Fresnel number. In Table 4 we compare the Fresnel number ($\frac{R^2}{\lambda z}$) for the inner occulter mask used in the laboratory with two design reference missions at 600 nm. THEIA [9] is a flagship-class mission designed for a 4-m telescope, and operating at two distances corresponding to a red-band and a blue-band set of wavelengths to reduce the size of the occulter as much as possible, with 600 nm corresponding to the blue-end observations at the far distance. O3 [10] is a probe-class mission designed for a smaller 1.1 m telescope. Its smaller aperture means that spectra are obtained via filtered photometric bands. The technological demonstrator design represents a mission featuring a small 5 m occulter flying relatively close-in at 670 km. Exo-S [11] is a probe class starshade mission also with a 1.1 m telescope developed during the Exo-S study in 2014-2015. As can be seen, our current lab mask is oversized by a factor of 25 to 50 compared to other typical flight designs. In the remainder of this section we describe a new mask design and a correspondingly larger experiment operating at a flight-like Fresnel number.

4.1. Scaled Occulter Mask Design. The procedure for designing the occulter mask is similar to that used previously and described in [12]. The main difference here is that we now have the ability to simultaneously optimize the apodization for the inner occulter and for the outer ring. This avoids the use of Babinet’s principle and reduces the computing time. As we’ll see, it also

TABLE 5. Summary of optimization parameters for inner and outer occulter shape design for the new scaled testbed.

Parameter	Space Scale
Separation distance, z	55,000 km
Outer Radius, R	43.7 m
Inner Radius, R_{inn}	21.9 m
Outer Opaque, b	35.0 m
Inner Opaque, a	14.9 m
Shadow Diameter, $2\rho_{max}$	6 m
Telescope Diameter, D	4 m
Smoothness, σ	0.1
Lower wavelength, λ_{min}	500 nm
Upper wavelength, λ_{max}	850 nm
Shadow discretization	40
Apodization discretization	6000
Wavelength discretization	17
Suppression constraint, 10^{-2c}	10^{-10}
Fresnel Number @ 600 nm	14.5

results in a higher performing mask (in terms of suppression and contrast). This new optimization finds the ideal apodization (accounting for both the inner and outer radii) via the linear program:

$$\begin{aligned}
\max : & \int_0^R A(r)rdr \\
\text{subj. to :} & -10^{-c} \leq \text{Re}(E_{occ}(\rho; \lambda)) \leq 10^{-c}, \forall 0 \leq \rho \leq \rho_{max}, \forall \lambda_{min} \leq \lambda \leq \lambda_{max} \\
& -10^{-c} \leq \text{Im}(E_{occ}(\rho; \lambda)) \leq 10^{-c}, \forall 0 \leq \rho \leq \rho_{max}, \forall \lambda_{min} \leq \lambda \leq \lambda_{max} \\
& A(r) = 0, 0 \leq r \leq a \\
& 0 \leq A(r) \leq 1, \forall 0 \leq r \leq R \\
& A'(r) \leq 0, \forall 0 \leq r \leq b \\
& A'(r) \geq 0, \forall b < r \leq R \\
(7) \quad & |A''(r)| \leq \sigma, \forall 0 \leq r \leq R
\end{aligned}$$

where $E_{occ}(\rho)$ and $A(r)$ are given in Eq. 1, σ represents the smoothness condition threshold, a the extent of the opaque central disk, b the extent of the outer annulus, and $2c$ the suppression performance level sought in the shadow. The formulation is infinite dimensional. We discretize wavelengths in the interval $[\lambda_{min}, \lambda_{max}]$, which defines the shadow suppression wavelength band. We also apply midpoint discretization for the radial coordinates, with r over the range $[0, R]$ and ρ over the range $[0, \rho_{max}]$ and use a trapezoidal scheme for numerical integration. The upper radial bound ρ_{max} on the shadow in the pupil plane defines the optimized dark hole portion of the shadow.

In Table 5, we list the parameters used in the optimization problem to obtain the apodization profile and corresponding petalized mask shown in Fig. 10 for the example suppression constraint of 10^{-10} .¹ The wavelength band $[\lambda_{min}, \lambda_{max}]$ is evenly discretized in 20 nm and 25 nm intervals to include the end wavelengths. We use midpoint discretization across the occulter radius r and across the shadow radius ρ . The outer ring is designed to be twice the radius of the inner occulter, and the inner tips of the outer petals are designed to start at four-fifths of the radial distance. The

¹In § 4.3 we will explore the performance for three different suppression constraints. However, all three have the same parameters listed in Table 5.

suppression constraint is introduced across each component of the electric field and thus setting $c = 5$ corresponds to a shadow intensity suppression of 10^{-10} . The struts are accounted for by introducing a multiplicative factor b on the apodization function to reduce the total transmission (taken to be 10% of the annulus for the design in Fig. 10).

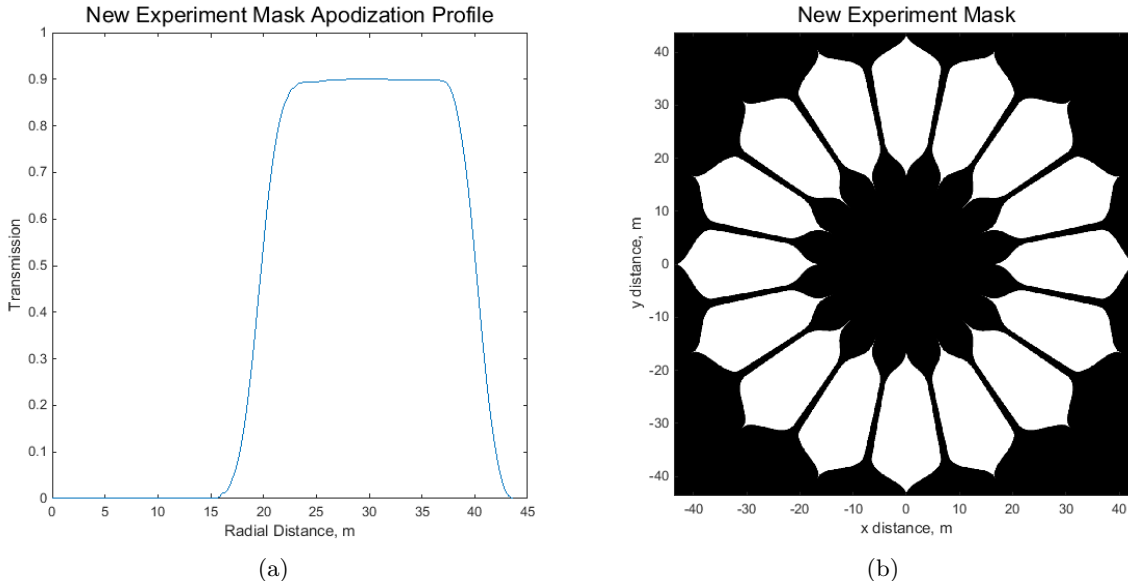


FIGURE 10. (a) Designed apodization profile including outer ring and struts. (b) Binary realization of mask profile.

The final line of Table 4 shows the Fresnel number of the inner occulter for the new flight design occulter, and its comparison with the other occulter designs. We see that at the newly designed dimensions, the occulter operates at a Fresnel number very similar to the THEIA design and represents a more realistic flight design than the oversized design used in the current propagation distance-limited experiment.

4.2. Laboratory Scaling. The floorspace of the new lab allows for a final propagation distance of 78 m, much larger than the current 10 m and enough to allow operation at flight Fresnel numbers. Figure 11 shows an updated layout for the new experimental testbed. In the current testbed, we use a full-size enclosure (i.e., one that is sufficiently large so that it would not clip the expanding beam) to mimic the space environment by eliminating ambient light and diffraction effects from finite edges. Due to the increased propagation distance in the updated testbed, a full-size enclosure connecting the source and the telescope optical table as used in the current testbed represents a significant structural engineering challenge. A more feasible approach is to connect the two enclosures that contain optical tables at either end via a smaller tunnel of diameter D , but this requires careful evaluation of the tunnel sizing (See [7, 8]). The occulter mask will be placed at a distance h from the artificial source and the camera is located at a distance z from the occulter mask. The total propagation distance available is given by $Z = h + z$.

Following the scaling discussion in §2, we first scale the design from space separation to laboratory separation by maintaining a constant Fresnel number as before. We designate the propagation distance for the space design as z_{space} . Then we scale to a new propagation distance z corresponding to lab dimensions by introducing a scaling factor $s = \sqrt{z_{\text{space}}/z}$. The new radius of the mask becomes $R' = R/s$. Thus, for the case of a direct spatial scaling with a plane wave input beam, the maximal mask size is achieved by increasing the separation distance z available in the laboratory.

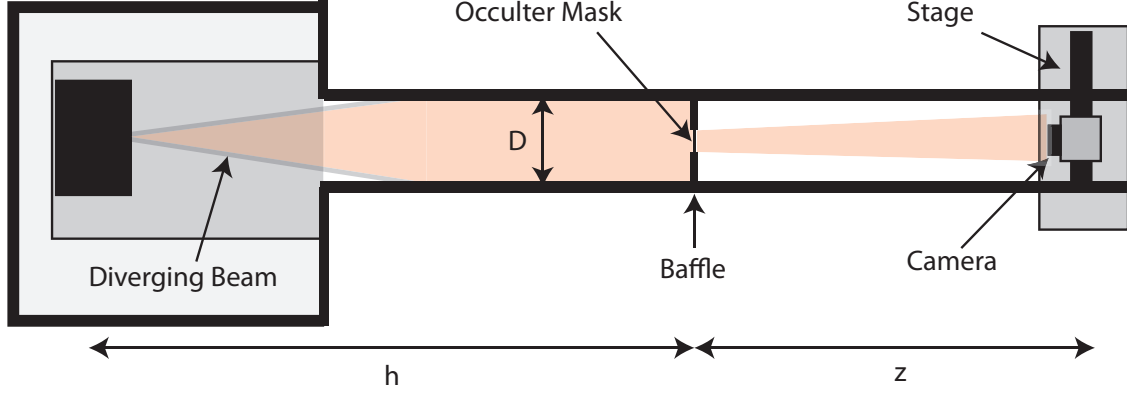


FIGURE 11. Layout of the new experimental testbed using a tunnel due to the increased total propagation distance

For a set total distance available Z , the source would be set to the minimum distance necessary to achieve a collimated beam and this would in turn maximize z . The finite size of the input collimated beam, however, can result in significant variation from the idealized infinite-extent planar input beam which can dominate the performance of the diffractive shadow—this effect is the likely limit on the performance of another occulter testbed [4, 5]. Additionally, any collimating optics used introduce wavefront errors that cannot be eliminated. Occulter performance is highly susceptible to phase errors at the occulter plane.

As described in § 2, to mitigate the diffractive effects related to a finite width collimated input beam, we design the testbed to operate with a diverging input beam. As with the current testbed we scale the design to account for a diverging input beam at the same separation distance as outlined in §2 by maintaining equivalent Fresnel numbers. For an occulter with a collimated input beam increasing the separation distance to the camera increases the mask size; however, for a diverging beam, setting the mask at a smaller distance h from the source results in a larger divergence and we must shrink the occulter mask's radius by a factor $\gamma = \sqrt{1 + z/h}$ such that $R'' = R'/\gamma$ compared to the equivalent collimated mask R' at the same separation distance z . We can show mathematically that the maximal occulter radius occurs at $z = h$. Consider the scaled occulter's radius expressed in terms of h for a fixed total available distance Z in relation to its designed radius R and separation in space z_{space} :

$$\begin{aligned}
 R'' &= \frac{R'}{\gamma} \\
 &= \frac{R/\sqrt{\frac{z_{\text{space}}}{z}}}{\sqrt{1 + z/h}} \\
 (8) \quad &= \frac{R}{\sqrt{z_{\text{space}}Z}} \sqrt{Z - h} \sqrt{h}
 \end{aligned}$$

To find the maximum we set the derivative with respect to h to zero:

$$\begin{aligned}
 0 &= \frac{dR''}{dh} = \frac{-\sqrt{h}}{2\sqrt{Z-h}} + \frac{Z-h}{2\sqrt{h}} \\
 (9) \quad &\therefore h = Z/2.
 \end{aligned}$$

We note that $\frac{d^2 R''}{dh^2} < 0, \forall 0 < h < Z$, thus ensuring $h = Z/2$ is indeed a maximum. This is verified in Figure 12 by plotting the inner scaled occulter's radius as a function of separation z for a fixed total distance $Z = 78$ m. The maximum occurs when $z = h = 39$ m as expected.

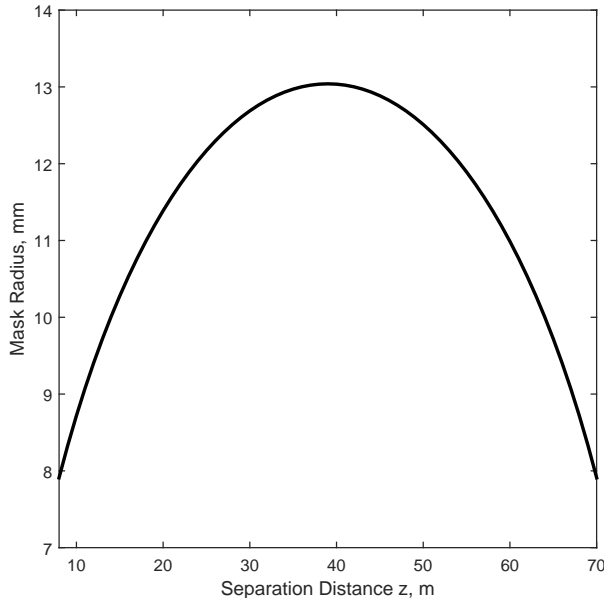


FIGURE 12. Scaling of the beam divergence by maintaining an 14.5 Fresnel number for a fixed 78 m total propagation distance, with varying occulter-telescope distances.

In Table 6, we summarize the scaling of the occulter parameters. We first show the parameters of the designed occulter at space dimensions then scale these parameters to the laboratory. We assume a total distance of 78 m is available and optimally set the divergence to maximize the size of the occulter mask, which assumes a 39 m distance from the source to the mask and a 39 m propagation distance past the mask. The intermediate scaling for the collimated case assumes a 39 m distance scaling for comparison purposes. In the final column, we show the resulting scaled parameters after application of the beam divergence. Scaling for a diverging beam results in shrinking the occulter mask while increasing the size of the shadow. We correspondingly increase the size of the aperture to still correspond to a 4 m space telescope. However, we expect that we will experiment with different aperture sizes to, among other things, find the optimal size to remain in the shadow during the long integrations.

4.3. Predicted Performance. In this section we present the predicted performance from the mask designed as described above. This includes the ideal performance absent any manufacturing limitations and errors as well as the best performance to be expected in the presence of laboratory errors. This allows us to set a goal for our predicted suppression and contrast for the TDEM milestone.

4.3.1. Ideal One-Dimensional Simulation. In this section, we describe the performance of the ideal optimized occulter apodization profiles with perfectly symmetric realizations. We calculate the performance of the laboratory mask under scaled conditions corresponding to a diverging input beam as described in Eq. 6. In § 4.1 we described the linear program and optimization parameters used to design the occulter apodization profile. To evaluate the electric field downstream from the inner occulter, we use the Babinet version of the one-dimensional Fresnel diffraction integral including the Jacobi-Anger expansion with the series summation of the first twenty non-zero Bessel terms with sixteen petals (setting $K = 20$ and $N = 16$). The physical dimensions for the optical propagation are listed for the diverging scale column in Table 6. The wavelength is set at 633 nm to match the monochromatic HeNe laser used for the experimental laboratory.

TABLE 6. Summary of scaled laboratory parameters.

Parameter	Space Design	Collimated Scale	Diverging Scale
Separation distance, z	55,000 km	39 m	39 m
Distance scale, s	1	1188	1188
Source distance, h	∞	∞	39 m
Divergence scale, γ	1	1	1.4
Inner radius, R_{inn}	21.9 m	18.4 mm	13 mm
Outer radius, R_{out}	43.7 m	36.8 mm	26 mm
Outer Opaque, b	35.0 m	29.5 mm	20.8 mm
Inner Opaque, a	14.9 m	12.6 mm	8.8 mm
Dark shadow radius, ρ_{dark}	3 m	2.5 mm	3.5 mm
Outer shadow radius, ρ_{out}	43.7 m	36.8 mm	52 mm
Telescope diameter	4 m	3.4 mm	4.8 mm
Inner Working Angle	82.1 mas	97.5 as	69.0 as
Outer Working Angle	131 mas	156 as	110 as

The simulation results are shown in Fig. 13. The suppression-calibrated shadow intensity at the pupil plane is shown in Fig. 13(a), the contrast calibrated point spread function at the image plane is shown in Fig. 13(b), and the stretched image of the Fig. 13(b) is shown in Fig. 13(c). The azimuthal average curve for the suppression is shown in Fig. 13(d) and for the contrast in Fig. 13(e). The solid red line in Fig. 13(d) indicates the extent of the aperture for the diverging beam and solid red lines in Fig. 13(e) indicate the annular working region. The resulting mean suppression over a 4-m telescope centered in the occulter shadow is 10^{-11} , and the resulting mean contrast over a 4-m telescope centered in the occulter shadow is $10^{-13.4}$.

TABLE 7. Summary of sample sizes across the occulter plane representing different feature accuracies.

Feature Size, δR	Number of Samples, $n \times n$	Anti-Aliasing, $g \times g$
0.25 μm	5200 \times 5200	40 \times 40
0.5 μm	5200 \times 5200	20 \times 20
1.0 μm	5200 \times 5200	10 \times 10
2.0 μm	5200 \times 5200	5 \times 5
5.0 μm	5200 \times 5200	2 \times 2

4.3.2. *Feature Accuracy.* The simulated performance of the occulter mask in § 4.3.1 assumed a perfect realization using sixteen petals. As described in § 3.3, for a proper assessment of laboratory performance it is necessary to simulate the suppression and contrast of a realizable mask with expected feature accuracy in the manufacture of the mask. To do so we follow the same procedure as for our previous mask to model various feature accuracies by utilizing an anti-aliasing technique to reduce the number of grid points necessary to represent the occulter mask. We generate a two-dimensional mask model with $n \times n$ samples and allow one pixel (or sample) via a *gtimesg* anti-aliasing in order to approximate a higher-resolution grid than would be numerically tractable to fully simulate as a binary mask. This is achieved by computing a pattern of white and black squares over an area and determining the black fraction of the total area to obtain a gray approximation. Thus, a mask with $n \times n$ samples which uses a $g \times g$ anti-aliasing approximates a mask with feature size of $\delta R = 2R/ng$, where R is the radius of the mask to the outer edge.

For example, the diameter of the new mask for the lab is 52 mm. When we set the number of samples to 5200 \times 5200, then 1 sample (pixel) represents 10 micron ($2R/n = 52\text{mm}/5200 =$

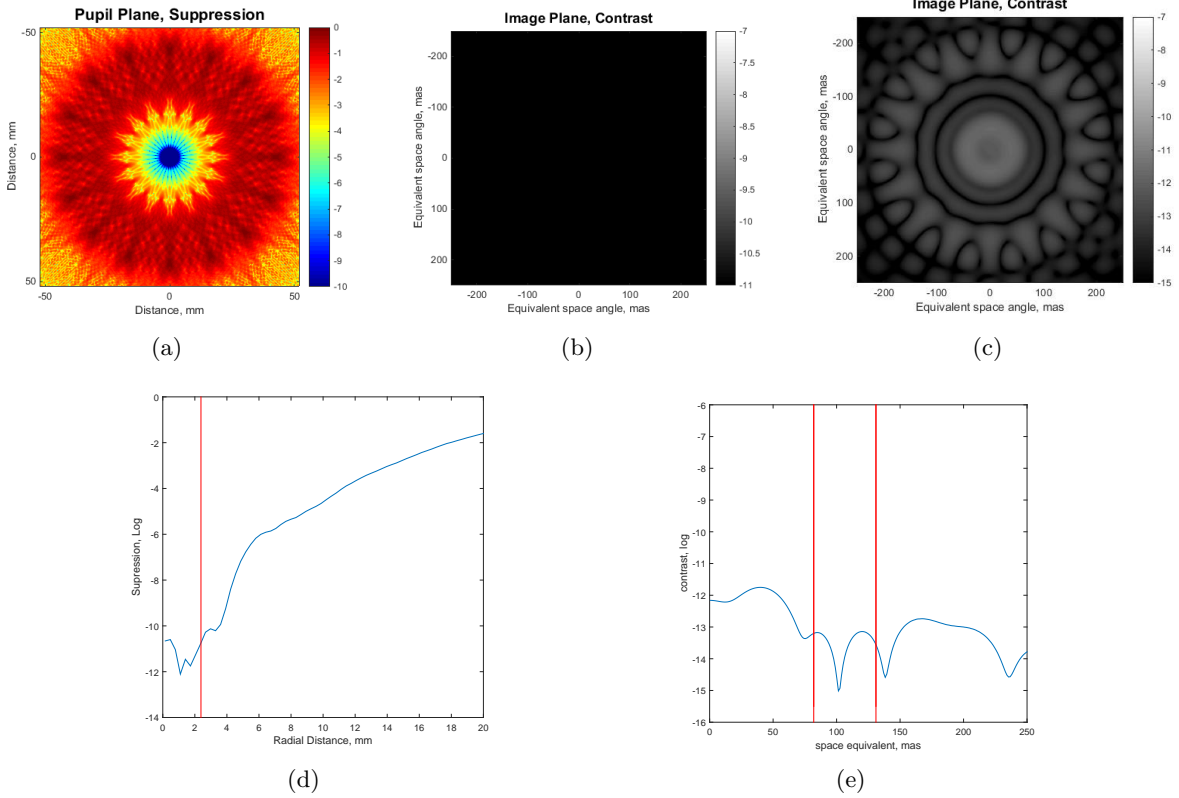


FIGURE 13. Effect on performance of ideal mask under diverging input beam laboratory conditions: (a) Suppression at the laboratory pupil plane for a diverging input beam. (b) Contrast at the laboratory image plane for a diverging input beam (c) Stretched image of contrast at the laboratory image plane. (d) Azimuthal average suppression across pupil plane. The solid red line indicates the extent of the aperture at the shadow, with a mean suppression across this aperture of 10^{-11} . (e) Azimuthal average contrast across the image plane with a diverging input beam. Solid red lines indicate the annular working region of the annulus. Mean contrast over the annular region for the diverging beam cases is $10^{-13.4}$.

0.01mm = 10micron). After that, we allow a $g \times g$ anti-aliasing subgrid at each pixel. When the anti-aliasing factor g is 10, the feature size is 1 micron. As a result, 1 pixel contains gray values of correspond to the black fraction of the total area with feature size 1 micron.

This feature size of points along the edges represents the accuracy of the polygons used in the CAD model supplied to MDL for manufacture. We summarize the model for different mask feature sizes in Table 7, where we have set $n = 5200$ and vary g to achieve the different feature accuracies.

Using these mask models across the occulter plane, we perform two-dimensional optical propagations and compare the results to those for the high-resolution mask. We compute the suppression at the pupil plane across the telescope aperture and the corresponding contrast in the annular working region for the different manufacturing feature accuracies. In Fig. 14 we show the two dimensional suppression-calibrated pupil and corresponding contrast-calibrated image planes at five representative feature sizes. In Fig. 14(a) and 14(b) the results are shown for the $0.25 \mu\text{m}$ model. This model represents performance close to the ideal model. The feature size is increased to $0.5 \mu\text{m}$, $1.0 \mu\text{m}$, $2.0 \mu\text{m}$, and $5 \mu\text{m}$. Figure 14(c) shows the suppression at the laboratory pupil plane for $0.5 \mu\text{m}$ features and Fig. 14(d) shows the corresponding contrast at the laboratory image plane.

Likewise, Figs. 14(e) through 14(j) show the suppression and contrast at the other feature sizes. The differences in suppression are small until $1.0\ \mu\text{m}$. The dark hole across the pupil plane changes slightly at $2.0\ \mu\text{m}$ and disappears almost entirely at $5.0\ \mu\text{m}$. Similarly, in the image plane, the contrast level become worse when the feature sizes are increased. The intensity of the central lobe has increased while its wings now completely cover the dark annular region at $5.0\ \mu\text{m}$. Recall that our previous lab mask had a feature accuracy of roughly $2.4\ \mu\text{m}$.

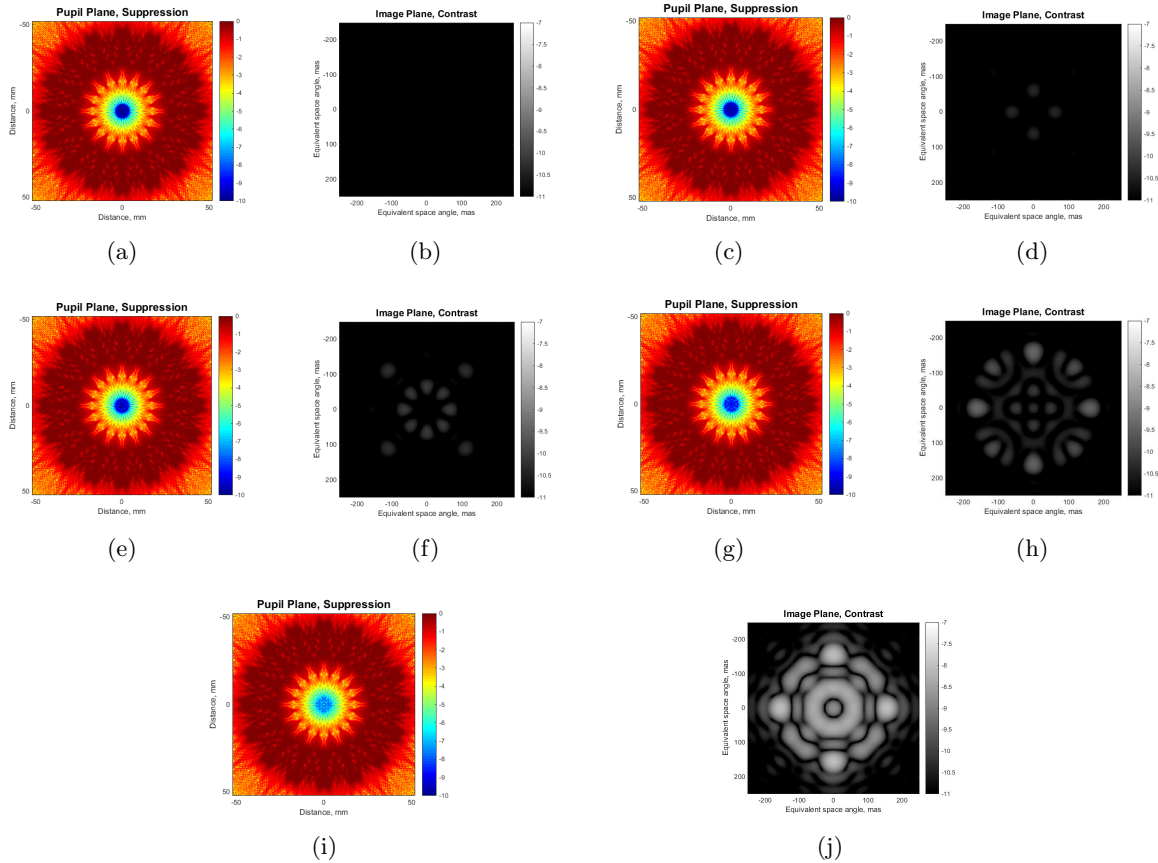


FIGURE 14. Performance of the laboratory mask using different mask manufacturing feature accuracies. (a) Suppression at the laboratory pupil plane for $0.25\ \mu\text{m}$ features (b) Contrast at the laboratory image plane for $0.25\ \mu\text{m}$ features. (c) Suppression at the laboratory pupil plane for $0.5\ \mu\text{m}$ features. (d) Contrast at the laboratory image plane for $0.5\ \mu\text{m}$ features. (e) Suppression at the laboratory pupil plane for $1.0\ \mu\text{m}$ features. (f) Contrast at the laboratory image plane for $1.0\ \mu\text{m}$ features. (g) Suppression at the laboratory pupil plane for $2.0\ \mu\text{m}$ features. (h) Contrast at the laboratory image plane for $2.0\ \mu\text{m}$ features. (i) Suppression at the laboratory pupil plane for $5.0\ \mu\text{m}$ features. (j) Contrast at the laboratory image plane for $5.0\ \mu\text{m}$ features.

We also calculate azimuthally averaged suppression and contrast curves in Figs. 15(a) and 15(b) respectively. All of the cases featured in the two-dimensional plots above are presented and compared to the ideal case. We see monotonic worsening of performance from the ideal case as the feature size is increased. Based on conversations with MDL, we expect that $0.25\ \mu\text{m}$ feature size is the smallest achievable resolution in the mask manufacturing process and is therefore likely the

indicator of the best possible performance. The performance at $0.25 \mu\text{m}$ is worse than the ideal design but still satisfies our target suppression.

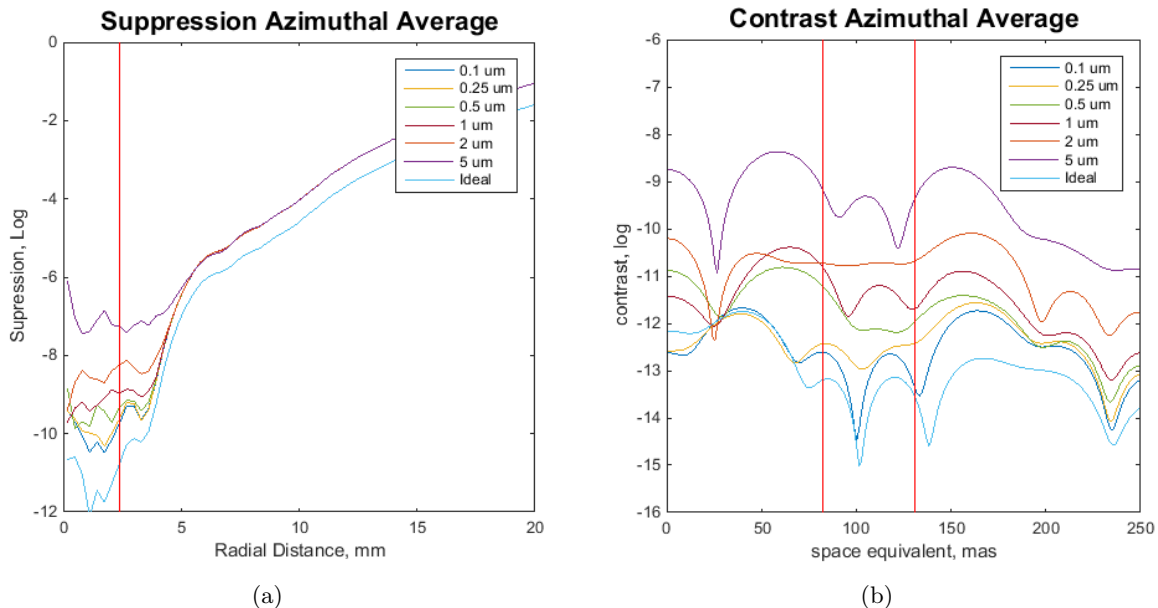


FIGURE 15. Performance comparison among laboratory masks using different mask manufacturing feature accuracies. (a) Azimuthally averaged suppression performance. Solid red line indicates extent of telescope aperture across which mean suppression is reported. (b) Azimuthally averaged contrast performance. Solid red lines indicate annular working region across which mean contrast is reported.

In Fig. 16 we show the degradation in average suppression and contrast vs. feature accuracy as we vary the suppression constraint in the optimization parameters shown in Table 5 for three cases of 10^{-11} , 10^{-10} , and 10^{-9} . Keeping all other parameters the same, we find three different apodization profiles and convert them to 2D model with the same feature sizes as in Table 7. In Fig. 16(a), the mean suppression results across the telescope aperture with different suppression constraints are shown and in Fig. 16(b) we show the corresponding contrast performance. The dashed green line indicates a suppression constraint of 10^{-9} , the dashed blue line indicates a suppression constraint of 10^{-10} , and the dashed purple line indicates a suppression constraint of 10^{-11} . These results show that while the mask with deeper suppression is slightly more sensitive to feature accuracy, the performance of all the masks is roughly the same above a feature accuracy of $0.5 \mu\text{m}$. Since our expectation is that the accuracy will be between 0.25 and $0.5 \mu\text{m}$, these results imply we should manufacture the mask with the deepest suppression (10^{-11}). Should the feature accuracy be above $0.5 \mu\text{m}$, there is no penalty to choosing the mask with the best contrast.

4.3.3. Broadband Simulation. As outlined in the Table 5, the occulter shadow was optimized at 20 nm and 25 nm intervals over the band 500-850 nm. It is important to numerically validate the performance of the occulter mask at wavelengths between those for which the occulter mask was specifically optimized to determine the suitability of the design for a broadband input and to obtain an estimate of its performance against which experimental results can be compared. We do so for the three different suppression constraints and two feature sizes, 0.25 and $0.5 \mu\text{m}$ and compare to the ideal apodized response. In Fig. 17 we plot the mean suppression across the dark hole as a function of wavelength with different suppression constraints. We plot the curves at 10

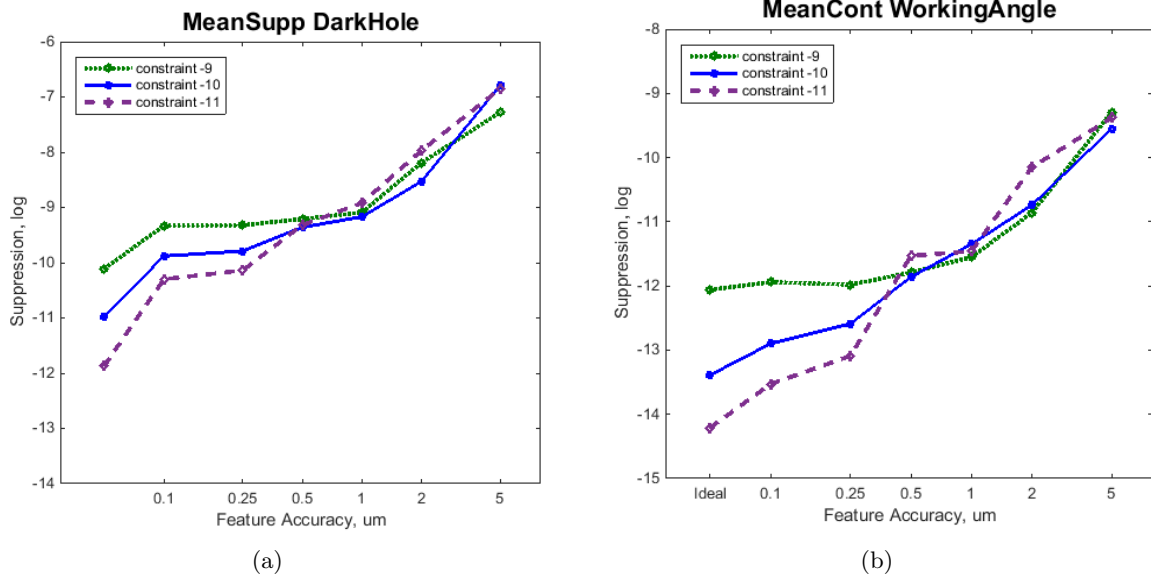


FIGURE 16. (a) Mean suppression at dark hole with different manufacturing feature size and different suppression constraint. (b) Mean contrast at annular working region with different manufacturing feature size and different suppression constraint. Dashed green line indicates suppression constraint of 10^{-9} , dashed blue line indicates suppression constraint of 10^{-10} , dashed purple line indicates suppression constraints as 10^{-11} .

nm intervals from 500 nm to 850 nm, covering both the optimized wavelengths and also the non-optimized wavelengths lying between the working wavelengths. Figure 17(a) shows the ideal case, Fig. 17(b) shows feature accuracy of $0.25 \mu\text{m}$, and Fig. 17(c) shows feature accuracy of $0.5 \mu\text{m}$. In Fig. 17(a) the suppression shows better performance than the suppression constraint at the given wavelength except 500 nm to 550 nm. In Fig. 17(b) the amount of suppression decrease is larger for the suppression constraint 10^{-11} . In Fig. 17(c) the suppression shows nearly similar levels at different suppression constraints as expected from Fig. 16. In Fig. 18 we plot the mean contrast across the dark annular working region as a function of wavelength. The trend of the results are also similar.

4.3.4. Edge Perturbations. The analysis in the previous two sections considered only symmetric edge feature accuracies defined by the regular polygons used in the shape definition. These deterministic models are symmetric, except for small quantization errors arising from translation of a sixteen-fold circularly symmetric pattern to a rectangular grid, and therefore represent an optimistic bound on performance. We now consider the effect on performance due to the loss of symmetry that arises from random perturbations at the mask edges that model manufacturing defects.

To calculate random edge perturbations we consider all of the gray contour pixels which represent the petal edge across the mask and introduce deviations. We define each gray contour pixel along a given petal indexed by k by the set $\mathcal{C}^k = \{c_i^k | 0 < c_i^k < 1, c_i^k \in R\}$ with each set containing N_k elements representing the number of grid points along the petal contour. We generate an edge error from the set $\mathcal{E}^k = \{e_i^k | e_i^k \in R\}$, where e_i^k is a Gaussian random number with mean zero and target standard deviation σ , and add it as edge perturbations for each petal. We thus define a new set of error points $\bar{\mathcal{C}}^k = \{\bar{c}_i^k | 0 < \bar{c}_i^k < 1, \bar{c}_i^k \in R\}$ for each petal k by addition of the generated

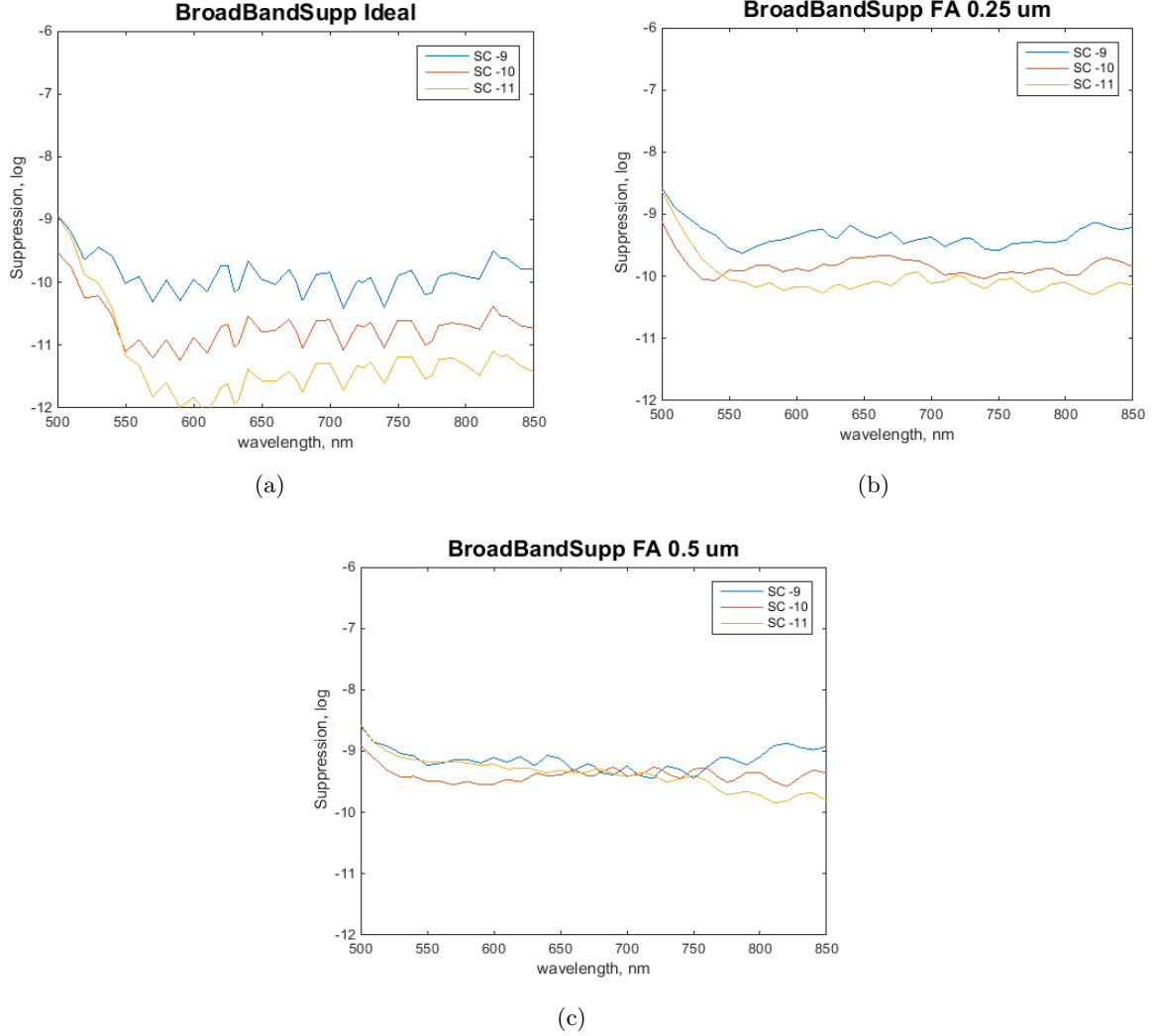


FIGURE 17. Suppression performance with different suppression constraint as a function of wavelength. (a) Ideal case (b) Feature accuracy 0.25 μm . (c) Feature accuracy 0.5 μm .

stochastic sequence and conversion of the RMS error to an appropriate gray-scale value:

$$(10) \quad \tilde{c}_i^k = c_i^k + \frac{\pi(e_i^k)^2}{(g\delta R)^2} \text{sgn}(e_i^k), \quad \forall i \in \{1 \dots N_k\}.$$

To avoid unphysical effects, we maintain the condition that $0 < \tilde{c}_i^k < 1$ by setting any negative values to 0 and any numbers greater than unity to 1.

We consider two feature accuracies (0.25 μm and 0.5 μm) and the three different suppression constraints. In Fig. 19(a) we show suppression vs. the standard deviation of the edge perturbation at 0.25 μm and 0.5 μm feature accuracy with different suppression constraints. In Figure 19(b) we show the corresponding contrast vs. edge perturbation. The solid lines represents 0.5 μm feature accuracy and the dashed lines indicate 0.25 μm feature accuracy. We see that with increasing edge perturbations there is increased diffraction along the occulter edges thus degrading performance. Above roughly 1 μm , the three different suppression constraints behave about the same. Based on conversations with MDL we believe that we can reasonably expect the random edge perturbations

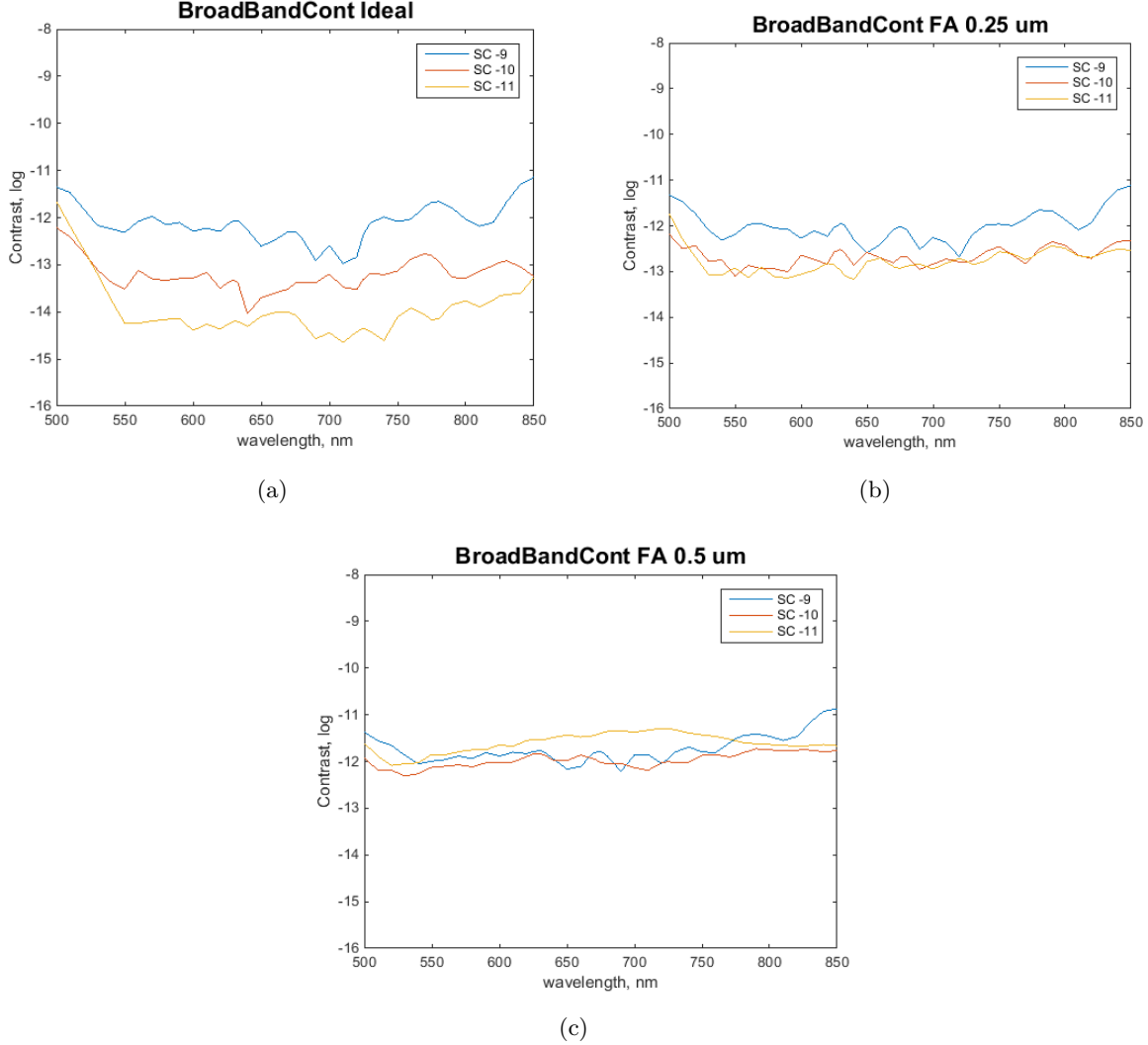


FIGURE 18. Contrast performance with different suppression constraint as a function of wavelength. (a) Ideal case (b) Feature accuracy $0.25 \mu\text{m}$. (c) Feature accuracy $0.5 \mu\text{m}$.

to be less than $1 \mu\text{m}$, hopefully less than $0.5 \mu\text{m}$. These results again point to selecting the 10^{-11} mask and supports our choice of milestone value of 10^{-9} suppression, leaving margin for other errors.

4.3.5. Beam Misalignment, Pinhole Phase Error, and Mask Tilt. In addition to the mask manufacturing errors described above, there are several laboratory tolerances that need to be accounted for in making contrast prediction, or that need to be controlled to appropriate levels to maintain our goal of 10^{-9} suppression. These errors are described in detail in [7, 8, 13]. The first, beam misalignment, is found by first modifying the two-dimensional Fresnel integral to include the Gaussian input beam from the pinhole and non-zero phase across the mask. We then simulate a misaligned input beam across the occulter mask by displacing the optical axis of the pinhole from the occulter plane to detector plane. From the simulation results we find a small amount of light leakage at the inner ring of the occulter mask due to misalignment of the input beam. When the misalignment is less than 2 mm the effect on contrast is negligible.

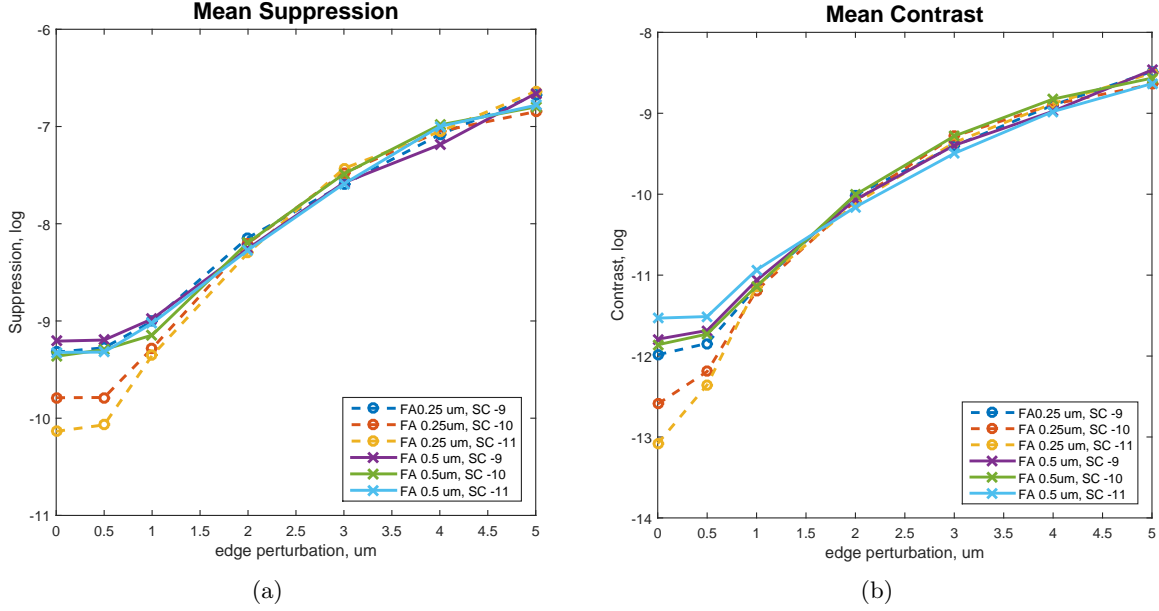


FIGURE 19. (a) Suppression at $0.25 \mu\text{m}$ and $0.5 \mu\text{m}$ feature accuracy vs. edge perturbation size with different suppression constraints. (b) Contrast at $0.25 \mu\text{m}$ and $0.5 \mu\text{m}$ feature accuracy vs. edge perturbation size with different suppression constraint. Solid line represents $0.25 \mu\text{m}$ feature accuracy and dashed line indicates $0.5 \mu\text{m}$ feature accuracy.

We introduce pure phase aberrations across the pinhole plane by generating a two-dimensional aberrated matrix at this position with a given spectral density. We characterize the error by its rms value found by averaging over the matrix. Because of the spatial filtering effect of the pinhole, high-frequency phase aberrations from the optics are filtered out. Therefore, even large aberrations on the order of $\lambda/4$ or greater have a small effect on the performance metrics. The results suggest that the pinhole filters aberrations induced by the upstream optical surfaces very well.

To model the loss of symmetry due to a mask tilt, a rotation and in-plane projection can be applied to the occulter mask. We simulate mask tilt by shrinking the mask along the x-axis while maintaining the mask apodization information at each pixel. This model only consider the amplitude effect of the mask tilt. The result is that the performance of the mask will be degraded when the mask tilt is larger than 1 deg. Our experience in the existing lab shows us that this tilt should be easy to meet.

Figure 20 shows the net suppression and contrast of the selected mask ($0.25 \mu\text{m}$ features and 10^{-11} suppression) including all of the above errors. Table 8 shows the selected values for each of the errors. For these values we find that we can still expect a predicted suppression of better than 10^{-9} and the corresponding contrast. All of the values in the table we can reasonably expect to achieve in the laboratory, giving confidence in our milestone value. Note also that we are planning on using a thinner mask than previously ($1 \mu\text{m}$ rather than $50 \mu\text{m}$). While we no longer believe the error is due to reflections from mask edges, this still minimizes the chances of glints and avoids large aspect ratio features.

4.3.6. *Wavefront Error.* The remaining source of error will be wavefront variations due to air motion and density inhomogeneities in the tubes. The laboratory enclosure will be operating at room temperature in a non-stabilized environment. As such, it is possible for temperature gradients to develop, which may result in atmospheric effects due to variations in refractive index across the

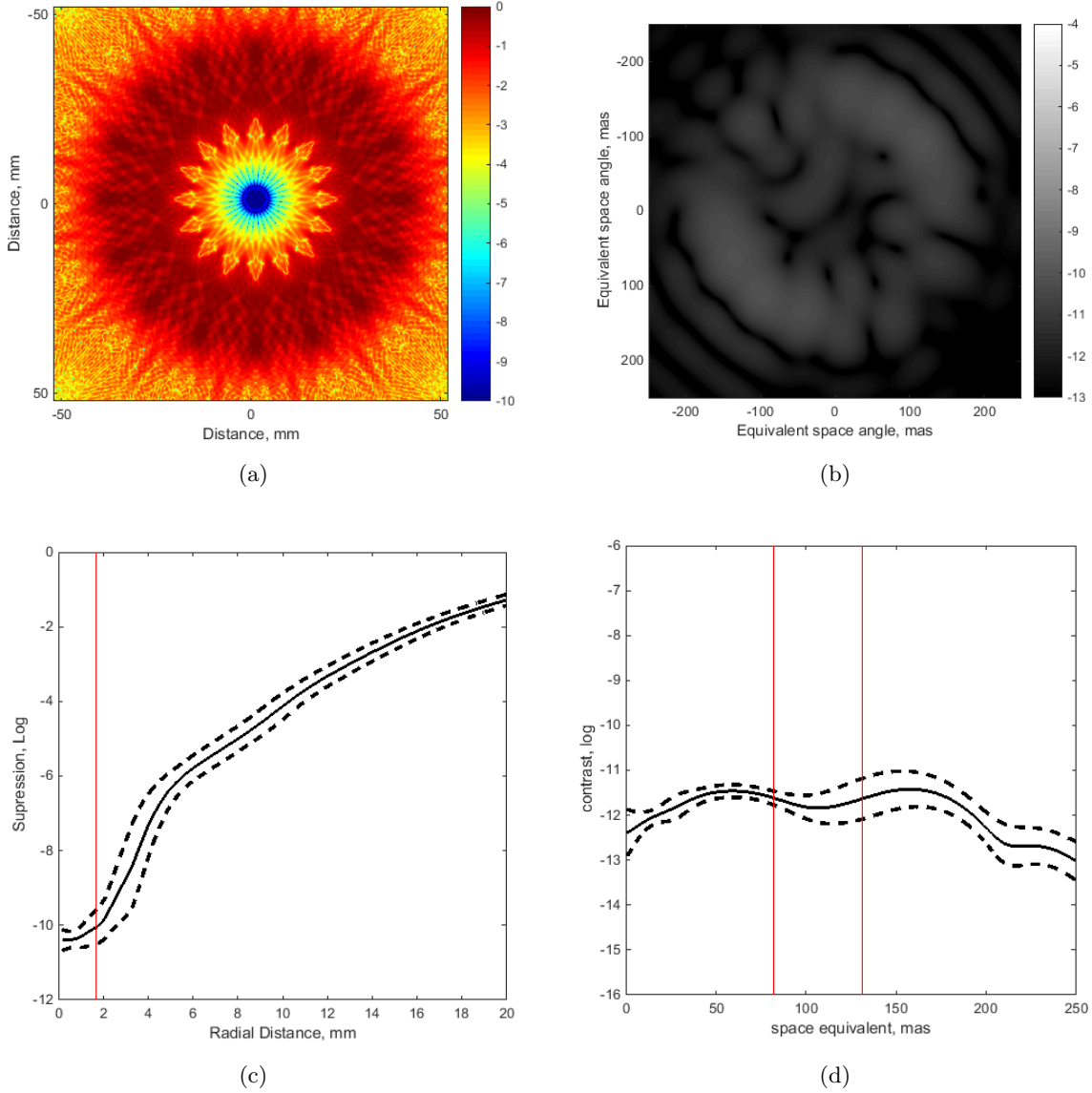


FIGURE 20. Performance of the laboratory mask using combined error analysis (a) Worst case suppression map (b) Worst case contrast map (c) Suppression profile with 50 runs Monte Carlo simulation (d) Contrast profile with 50 runs Monte Carlo simulation. Dashed lines indicate the 1 sigma standard deviation of the simulation.

propagation direction. Straightforward analyses such as those in [7, 8, 13] using simple power law wavefront error shows that the suppression and contrast are extremely sensitive to wavefront aberrations. Wavefront error with an rms as small as 0.1 nm can result in a loss of suppression beyond 10^{-9} . However, the system is also sensitive to the spatial scales assumed. Further modeling is necessary to understand the response to turbulent and laminar air motion. Careful modeling of the experiment is required to reliably predict the air motion and resulting wavefront aberrations. These will be performed as part of the study in order to ensure our models match our eventual measurements. In addition, we plan to perform wavefront measurements directly on a representative tube segment in a similar environment to bound the wavefront error problem.

TABLE 8. Summary of realistic error parameters for simulation of laboratory environment.

Error Parameter	Budget
Feature Accuracy	0.25 μm
Edge Perturbation	0.5 μm
Optical Aberrations	$\lambda/10 \approx 60 \text{ nm}$
Diagonal Beam Misalignment	2 mm
Mask Tilt	1 deg
Mask Thickness	1 μm

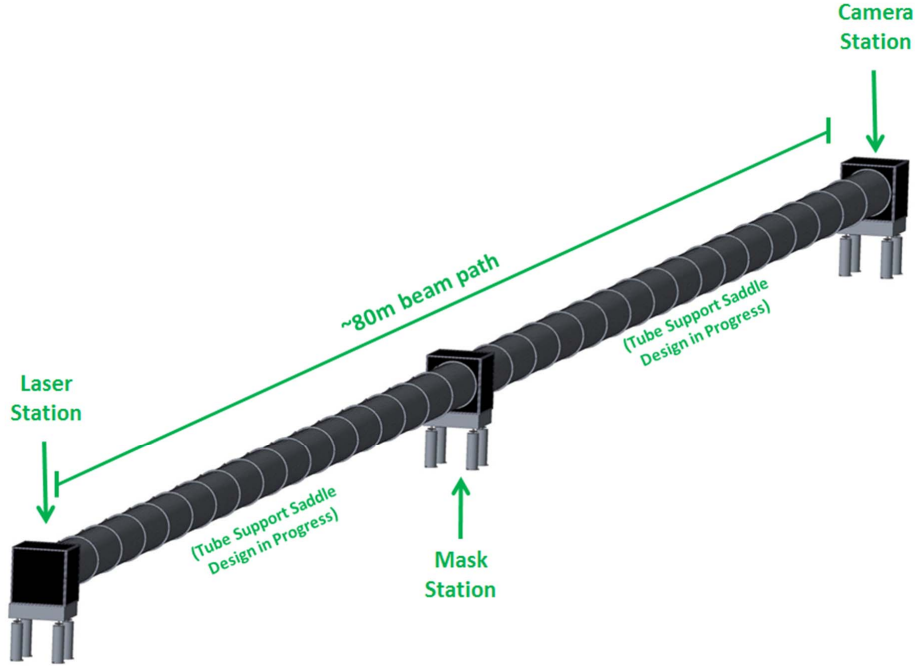


FIGURE 21. Schematic layout of the new lab facility.

4.4. **Experiment Design.** The new laboratory facility will be located in an 80 m long hallway in the basement of the Frick Chemistry building on Princeton University’s campus. The location is climate-controlled with minimal foot traffic. The basement location provides a stable environment for the optical tables. We ran a simple vibration test to confirm adequate stability of the space. The process was as follows:

- A sheet of paper was securely taped flat against one far wall of the lab hallway. The paper had a specific, known target pattern of circles at discrete sizes and spacings to serve as both:
 - Fixed referenced points relative to which the beam drifts
 - Scaling references (to determine the length scale of each pixel on the final drift video)
- A HeNe laser was secured onto on a heavy, stable baseplate at one the opposite far end of the lab hallway. It was pointed all the way down the hall at the target.
- The laser formed a spot on the target with a discernable edge. A visual inspection over several minutes confirmed that the edge did not jitter on the millimeter scale, even with someone walking near the laser baseplate.
- A video camera was arranged on a tripod just below the beam and pointed towards the spot (on the target).

- Video footage of the spot drifting on the target was taken for a full 24-hour diurnal cycle. This slow, continuous drift (on the order of several millimeters over 24 hours) was attributed to small, slow relative motion (combined translation, tip and tilt) of the opposite sides of the hallway, resultant from the diurnal thermal contraction and expansion of the building itself.
- The video was analyzed to determine the worst-case magnitude of translation over the 24-hour period. The target circles of known size were used to determine the length scale of each video pixel. This length scale was compensated for the slightly skewed perspective (filming upwards at the target from under the beam). The location of the beam was considered to be the instantaneous centroid of the HeNe spot. Multiple RGB luminance threshold values were tried to confirm that the centroid was insensitive to chosen threshold.

These tests showed that short term jitter is negligible (below the submillimeter measurement resolution) and that slow drift over 24 hours is on the order of 1.5 to 3 mm. The key requirement is that the differential drift between the occulter mask and the camera be less than the margin in the shadow size (as in space). The shadow diameter of the design in the previous section is 7 mm. Thus, based on the drift measurements on shorter timescales, this limits exposures before recentering to between 1 and 2 hours. The combination of laser power, aperture size, and integration time will be chosen to ensure the camera stays in the shadow over these integration times.

Differential motion between the laser/pinhole and mask as well as tip/tilt of the laser has negligible effect on the shadow and contrast due to the diverging beam. These small motions only change the location of the beam on the mask resulting in negligible effects on suppression.

The facility will be composed of a long, enclosed tube with three stations, one for the laser and pinhole, one midway for the starshade mask, and one at the end for the camera. This is different from the current facility where the entire experiment is enclosed. Figure 21 shows a schematic diagram of the layout. Simulations described in [7, 8] show that a tube diameter of 1 m or greater is adequate for diffraction effects not to affect the shadow at the 10^{-9} suppression level. The tube is made up of 34 2.2m segments of 0.965 m diameter (the largest allowable by the facility fire code). They are standard ductwork tubes made from spiral-wound Galvanneal sheet joined by Galvanneal Accuflanges and light-tight Neoprene gaskets. The flanges double as baffling along the length of the tube. The interior of the tube is painted matte black with a very low reflectivity paint. 13 possible paint combinations were selected based on specifications and spectrophotometer reflectance tests were performed at JPL to choose the best paint. Figure 22 shows a schematic of a tube segment. The tubes will be supported along their length by support saddles from simple 80/20 suspensions. A subscale mockup of a prototype saddle is shown in Fig. 23.

Diagrams of the workstation enclosures for the laser, mask, and camera are shown in Fig. 24. The enclosures are semi-custom versions of Newport's standard LTE-44-4 ($4' \times 4' \times 4'$) light-tight enclosure. The standard hardboard panels are being replaced with sturdy low-reflectance matte black acrylic panels. The tube opening will be custom machined and rigidly attached to the tube flanges. The enclosures sit on semicustom $4' \times 4'$ version of Newport's RS2000 research grade table.

5. SUCCESS CRITERIA

Unlike our past TDEMs, where multiple measurements were needed followed by an involved statistical analysis, in this TDEM the measurements and thus success criteria are fairly simple and somewhat similar to early coronagraph milestones where a specific contrast goal was achieved. We will take a sequence of at least 5 measurements of suppression and contrast. These measurements will be taken on separate days under varying conditions. Success is measured by achieving the target suppression and corresponding contrast (depending on final aperture size) on each of the 5 successive experimental runs.

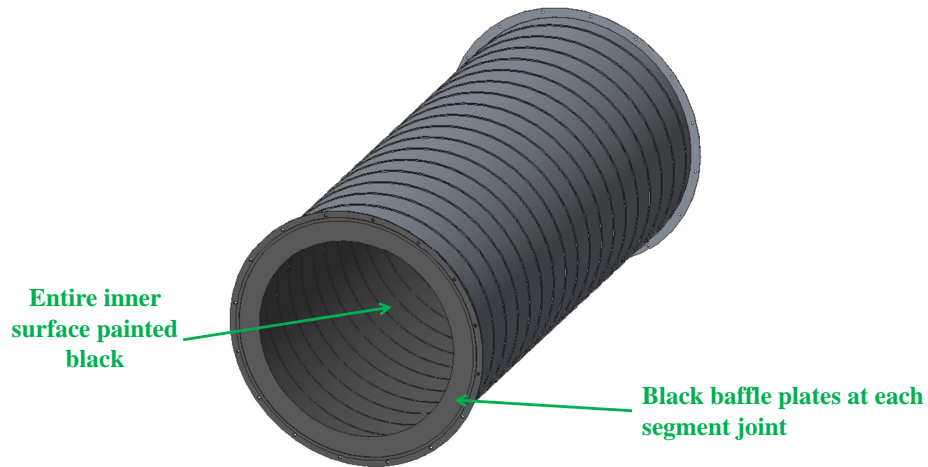


FIGURE 22. Schematic of tube segment.



FIGURE 23. Prototype model for the tube support saddles.

We will use two different laser sources to create the diverging beam as an artificial star, one monochromatic and one multichannel. For initial tests we will use the lasers from our previous experiment, a 2 mW HeNe laser operating at 633 nm and a four channel fibre-coupled laser source operating 520 nm and 638 nm. Final choice of higher-power and multi-channel lasers is still to be determined.

The suppression measurements will follow the same process described earlier for the previous facility. The telephoto lens is removed and the camera scans the shadow on the long travel stage. A mosaic is created similar to Fig. 7. Each frame has a different exposure to keep the camera operating in the linear regime. As before, many frames are taken and stacked to reduce the noise. A median-combined dark consisting of at least 50 frames is subtracted from the measurement. The



FIGURE 24. Schematic of the enclosures for the end stations.

exact integration times and number of frames is to be determined depending upon the final camera choice, its read noise, and its linearity. Integration times and the number of stacked frames (as well as the camera choice) will be made to ensure a signal-to-noise on the suppression measurement in the dark hole of at least 3 (that is, the standard deviation about the mean suppression measurement is less than $1/3$ the mean).

Contrast is measured at the image plane with a camera focused on the point source, and is the ratio between the flux at each pixel in the image formed when the mask is in place and the flux of the peak pixel of the PSF without a mask. This measurement is taken by first centering the camera in the shadow of the occulter mask with the lens attached. In the previous experiment we set 1 sec of exposure time to get one contrast image at image plane. In the new experiment, the exposure time to get one contrast image without changing the laser power would be 55 sec. To get the average contrast image we usually need more than 1000 images. That's 2 days worth of exposure per test, and the plan to do five tests. The exposure time to get one suppression image without changing the laser power would be 9.2 hour. To get the average suppression image we usually need more than 50 images. That's nearly 20 days worth of exposure per test. In order to reduce the exposure time we are considering using a high power laser. One of the candidate is 20 mW laser. In this case, the exposure time to get one contrast image would be 5.5 sec and the exposure time to get one suppression image would be 55 min. We expect four days to be enough time to get suppression and contrast data for one test.

To convert to contrast, the mask is removed and short exposures are retaken to get an image of the point source. We use an ND 5 filter to avoid saturation of the point source image. In the previous experiment we set 0.1 sec of exposure time to get one light source image. In the new experiment the exposure time for one light source image would be 0.55 sec with no other changes. Measuring both suppression and contrast is useful as it allows for verification of the consistency of the results. Contrast measurements can indicate the limitations of the suppression performance of the occulter mask, as the source of any stray light can be directly observed. As with suppression, a sufficient number of exposures will be made to ensure a signal-to-noise of at least 3 on the contrast measurement.

6. CERTIFICATION

The PI will assemble a milestone certification data package for review by the ExEPTAC and the ExEP program. In the event of a consensus determination that the success criteria have been met, the project will submit the findings of the review board, together with the certification

data package, to NASA HQ for official certification of milestone compliance. In the event of a disagreement between the ExEP project and the ExEPTAC, NASA HQ will determine whether to accept the data package and certify compliance or request additional work.

The milestone certification data package will contain the following explanations, charts, and data products:

- (1) A narrative report, including a discussion of how each element of the milestone was met, and a narrative summary of the overall milestone achievement.
- (2) Description of the final lab design and the manufacture and assembly steps.
- (3) Description of the measurement and data collection process.
- (4) Description of the post-processing needed to determine suppression and contrast.
- (5) Description of the milestone determination and certification.

7. WORK PLAN AND SCHEDULE

Work is under way and we expect to complete the TDEM milestone by next year. As can be seen in this white paper, the analysis and design of the laboratory scaled mask is largely completed and indicates promising performance in suppression and contrast. The final analysis step is to revise our predictions on wavefront error. Nevertheless, we have completed what we expect to be the final mask design. We are holding off sending that to MDL until we complete the current experiments in the old lab to confirm the manufacturing tolerances. We expect to send them the CAD model for the mask in late October.

Again, as shown in this white paper, the laboratory design is largely complete. The support material has been delivered and the supports are complete. The tubes are arriving and we expect assembly to be completed by early November. The mid-station table has been ordered and the two end-station tables will be ordered in late October. The optical tables will then be installed and the laser, masks, camera and optics will be installed. We expect the entire installation to be completed with first light by mid-December. We also plan to perform wavefront measurements on a single tube in early December followed by wavefront measurements of the entire facility in January.

We expect the months of January and February to be spent on alignment and calibration with high-contrast experiments beginning by March 1. Our goal is to complete the final milestone measurements by the end April, 2016 with May and June spent writing the final report. Our expectation is to present the final results of the TDEM at the SPIE Astronomical Telescopes meeting in Edinburgh, Scotland in June of 2016.

TABLE 9. Summary of TDEM Milestones

Milestone Name	Completion Date
Final Performance Analysis	complete
Final Mask Design	complete
Final Lab Mechanical Design	complete
Tube Saddles Assembly Complete	complete
Mask Delivery	Oct. 30, 2015
Tube Assembly Complete	Nov. 10, 2015
Enclosure and Final Assembly Complete	Nov. 30, 2015
Wavefront Measurements	Dec. 1, 2015
Optical Assembly Complete	Dec. 17, 2015
Optical Alignment & Calibration Complete	Feb. 29, 2016
Final Milestone Measurement	April 27, 2016
Final Milestone Report Delivered	June 1, 2016

8. LIST OF ACRONYMS

AAS	American Astronomical Society
CAD	Computer Aided Design
CCD	Charge Coupled Device
DRIE	Deep Reactive Ion Etching
IWA	Inner Working Angle
OWA	Outer Working Angle
JPL	Jet Propulsion Laboratory
MDL	Microdevices Lab
NASA	National Aeronautics and Space Administration
O3	Occulting Ozone Observatory
RMS	Root Mean Square
TDEM	Technology Development for Exoplanet Missions
THEIA	Telescope for Habitable Exoplanets and Intergalactic Astronomy
TRL	Technology Readiness Level

REFERENCES

- [1] N. J. Kasdin, D. Lisman, S. B. Shaklan, M. W. Thomson, E. J. Cady, S. R. Martin, L. F. Marchen, R. J. Vanderbei, B. A. Macintosh, R. E. Rudd, D. Savransky, J. A. Mikula, and D. H. Lynch. Technology demonstration of star shade manufacturing for nasa’s exoplanet mission program. In *Proceedings of the SPIE Astronomical Telescopes and Instrumentation*, number 07 in 8442, 2012.
- [2] J.W. Goodman. *Introduction to Fourier Optics*. McGraw-Hill, 1996.
- [3] E. Schindhelm, A. Shipley, P. Oakley, D. Leviton, W. Cash, and G. Card. Laboratory studies of petal-shaped occulter. volume 6693, page 669305. SPIE, 2007.
- [4] Rocco Samuele, Tiffany Glassman, Adam M. J. Johnson, Rupal Varshneya, and Ann Shipley. Starlight suppression from the starshade testbed at ngas. volume 7440, page 744004. SPIE, 2009.
- [5] R. Samuele, R. Varshneya, T. P. Johnson, A. M. F. Johnson, and T. Glassman. Progress at the starshade testbed at Northrop Grumman Aerospace Systems: comparisons with computer simulations. In *Society of Photo-Optical Instrumentation Engineers (SPIE) Conference Series*, volume 7731 of *Presented at the Society of Photo-Optical Instrumentation Engineers (SPIE) Conference*, July 2010.
- [6] E. Cady, K. Balasubramanian, M. Carr, M. Dickie, P. Echternach, T. Groff, J. Kasdin, C. Laftchiev, M. McElwain, D. Sirbu, R. Vanderbei, and V. White. Progress on the occulter experiment at princeton. volume 7440. SPIE, 2009.
- [7] D. Sirbu, N. J. Kasdin, R. J. Vanderbei, and S. R. Martin. Diffractive analysis of limits of an occulter experiment. In *Proceedings of the SPIE Astronomical Telescopes and Instrumentation*, number 90 in 9143, 2014.
- [8] D. Sirbu, N. J. Kasdin, and R. J. Vanderbei. Diffraction-based sensitivity analysis for a laboratory occulter. *Optics Express*, 2015. Submitted.
- [9] N.J. Kasdin, E.J. Cady, P.J. Dumon, P.D. Lisman, S.B. Shaklan, R. Soummer, D.N. Spergel, and R.J. Vanderbei. Occulter design for theia. volume 7440. SPIE, 2009.
- [10] D. Savransky, D. N. Spergel, N. J. Kasdin, E. J. Cady, P. D. Lisman, S. H. Pravdo, S. B. Shaklan, and Y. Fujii. Occulting ozone observatory science overview. In *Proceedings of the SPIE Astronomical Instrumentation Conference*, number 88 in 7731, 2010.
- [11] Sara Seager, Margaret Turnbull, William Sparks, Mark Thomson, Stuart B Shaklan, Aki Roberge, Marc Kuchner, N Jeremy Kasdin, Shawn Domagal-Goldman, Webster Cash, et al. The Exo-S probe class starshade mission. In *SPIE Optical Engineering+Applications*, pages 96050W–96050W. International Society for Optics and Photonics, 2015.
- [12] E. J. Cady, N.J. Kasdin, R. Vanderbei, and R. Belikov. Optimal design of petal-shaped occulter for extra-solar planet detection. In *Proceedings of SPIE–Techniques and Instrumentation for Detection of Exoplanets III*, volume 6693, 2007.
- [13] D. Sirbu. *Occulter-Based High-Contrast Exoplanet Imaging: Design, Scaling, and Performance Verification*. PhD Dissertation, Princeton University.